UNIVERSITY OF SOUTHAMPTON

Mitigation of Anomalous signals in the CMS Barrel Electromagnetic Calorimeter

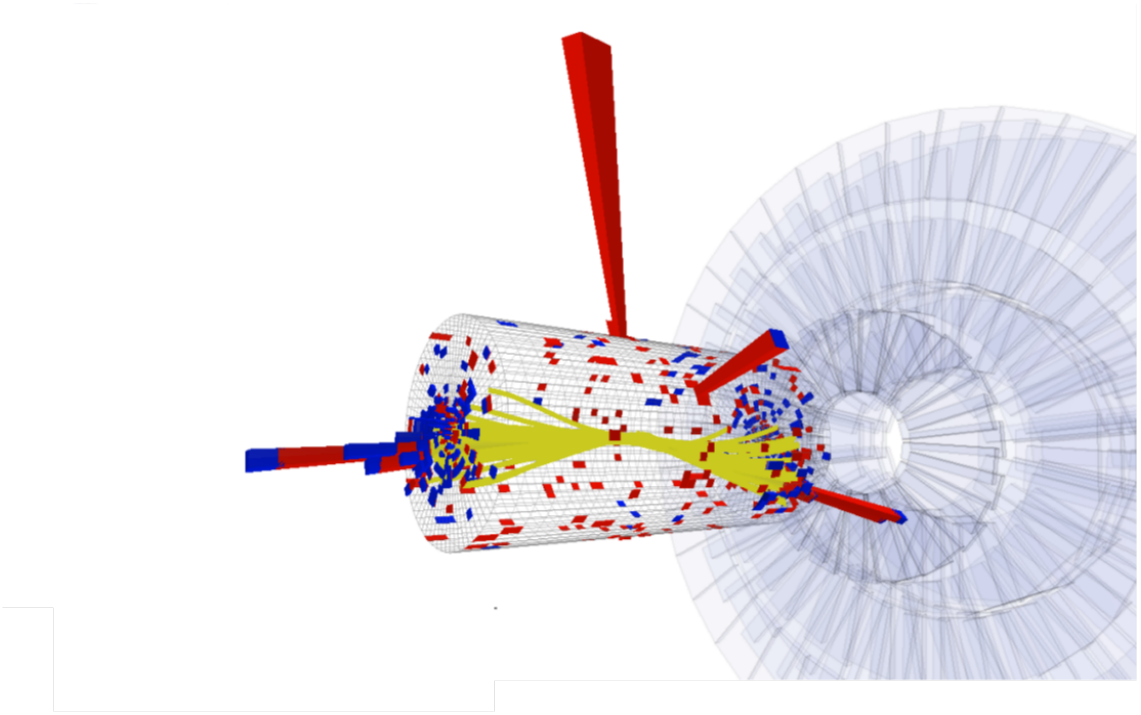

by

Ali Farzanehfar

A dissertation submitted in partial fulfilment for the degree of Master of Physics

in the
Faculty of Physical sciences and Engineering
The School of Physics and Astronomy

June 2015

Acknowledgements

I would like to thank my supervisors Drs. David Petyt and Dave Cockerill for their support, guidance, insight and patience throughout this research. In addition, I would like to thank Dr. Konstantinos Theofilatos for his part in discussions on the current pulse shape testing variable in CMS. This project would not be possible without the efforts of Prof. Stefano Moretti and the University of Southampton; they have my gratitude. Finally, I would like to thank Christopher Burr and Matthew Chapman for their abilities to absorb impacts from toy bullets and provide enlightening puns throughout the academic year.

UNIVERSITY OF SOUTHAMPTON

Abstract

Faculty of Physical sciences and Engineering
The School of Physics and Astronomy

Master of Physics

by Ali Farzanehfar

The characteristics and mitigation of large anomalous signals that have been observed in the CMS barrel Electromagnetic Calorimeter during proton-proton collisions are evaluated and investigated. The origin of these signals is summarised and their distinguishing features are described. A study is performed to investigate the effectiveness of signal pulse shape differences in distinguishing between anomalous signals and real electromagnetic energy deposits. To this end, the efficiency of a specific pulse shape dependent variable is evaluated using CMS data recorded in 2012. One particular limitation of this method is identified and several potential solutions are explored using a specially developed Monte Carlo simulation. The most effective solutions are identified and recommendations for their proposed implementation in CMS are provided.

Contents

List of Figures

List of Tables

This place is HUGE!...Now where is building 40?

Ali Farzanehfar, *Day 1 at the Meyrin site*

1 Introduction

The Standard Model of elementary particle physics describes, to a remarkable accuracy, the interactions between elementary particles that are known to exist. In order to confirm the descriptions of the standard model or other models, such as supersymmetry, the interactions between elementary particles have to be reproduced and observed.

The particle detectors at the CERN Large Hadron Collider (LHC) along with the collider itself were constructed to test these models and search for new physics [1, 2]. The experiments conducted by each detector are at the forefront of precision measurements of High Energy Particle physics[2]. Most recently this was demonstrated by the confirmation of the last remaining elementary particle predicted by the standard model, the Higgs boson. This was due to the observation of the decay of the Higgs boson (via $H \to \gamma\gamma$ and other channels) in two independent general purpose detectors at CERN, the ATLAS and CMS experiments[3, 4].

In order to provide accurate measurements of the properties of particle interactions and the particles themselves, the CERN detectors require large data samples. There is limited space is available for storing all the information that comes from the LHC detectors. Therefore, is essential that the components of each detector operate at optimal levels so that no unwanted data are stored and no useful data are ignored.

In the Compact Muon Solenoid (CMS), the component responsible for measuring electron (e) and photon (γ) events is the Electromagnetic Calorimeter (ECAL). This is the sub-detector responsible for providing precise measurements of photon energies in the $H \rightarrow \gamma\gamma$ decay channel, as well as the measurement of electron energies in $H \rightarrow ZZ \rightarrow 4l$ decays. All other measurements involving electrons or photons which are produced at the interaction point are also performed by the ECAL. Therefore, maintaining its excellent energy resolution[5] is essential for retaining useful and accurate physics data.

During the first LHC proton-proton ($p - p$) collisions in late 2009, anomalous isolated high energy signals were observed in the barrel region of the CMS ECAL. These signals, labelled *spikes* to reflect their local energy profile (Figure 1.1), appear as isolated signals with apparent energies up to several hundreds of GeV. Because they are isolated high energy signals in ECAL, spikes mimic the appearance of electrons or photons in CMS. If they occur at a high enough rate, these anomalous events create a significant problem for the efficient selection of real electrons and photons in CMS[6].

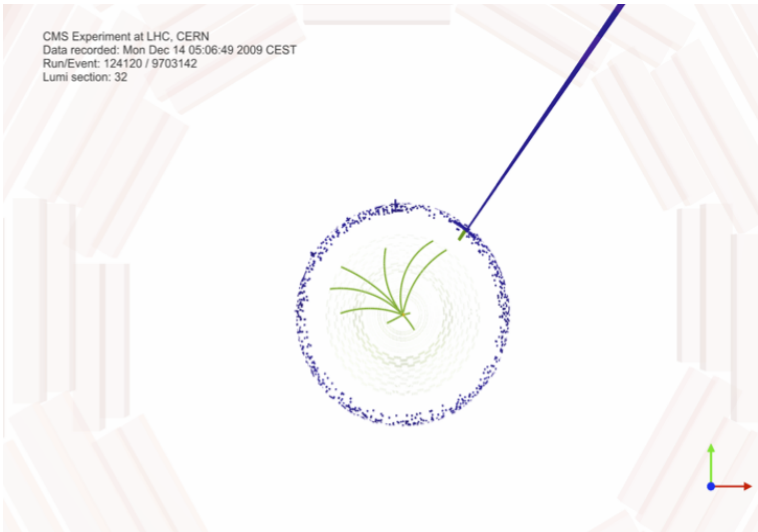

FIGURE 1.1: A cross sectional view of CMS showing an example of a spike signal in the ECAL. This was taken from a run with $\sqrt{s}$ =2.36 TeV and the signal corresponds to 690 GeV of transverse energy[6].

This research project was conducted to further optimise the mitigation of these anomalous signals. The origin and characteristics of spikes in CMS were studied. Current mitigation methods employed were understood and their performance, as well as their limitations were analysed. More advanced mitigation methods were investigated using the signal pulse shape using CMS data from $p - p$ collisions at the LHC in 2012. The current limits of these advanced mitigation techniques were identified. Attempts were made to optimise spike rejection techniques via the use of a specially developed Monte Carlo simulation. Finally, the results of these studies along with recommendation on the optimal spike rejection method to implement for the future are presented.

...I think I came close to dying only twice.

David Petyt, *While discussing cycling*

2

CMS and the ECAL

The Compact Muon Solenoid (CMS) (Figure 2.1) is one of two general purpose detectors located at the LHC at CERN. Located 100 m underground, the CMS detector weighs more than 14,000 tonnes and operates under the influence of a 3.8 T magnetic field[7].

The various layers of CMS each perform a precise set of functions. The innermost layer, the silicon tracker, is responsible for the measurement of the trajectories of charged particles emerging from the interaction point[7]. The next layer is the ECAL which is responsible for the measurement of photons and electrons. This is immediately followed by the Hadronic Calorimeter (HCAL) which is responsible for measurement of hadronic particles that are not stopped in the ECAL. The HCAL is encompassed by the muon system which measures muon trajectories and momenta[7].

As already mentioned, the ECAL is where the anomalous signals originate and so needs to be described in more detail.

2.1 The CMS ECAL

The CMS ECAL is a cylindrical detector split into a barrel section and two endcaps (Figure 2.2). This report will focus on the barrel ECAL.

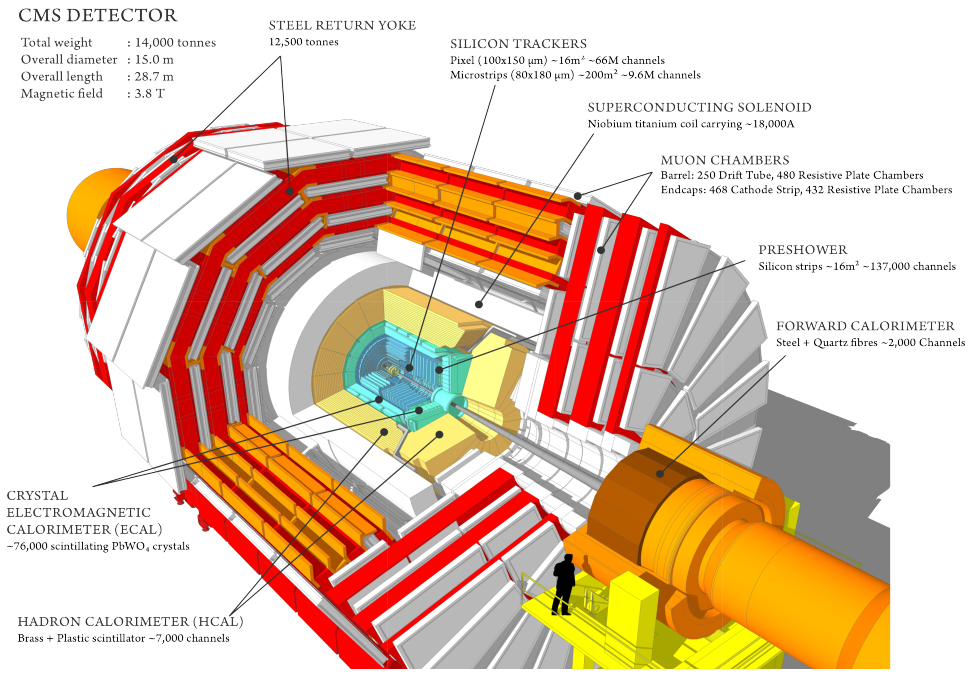

FIGURE 2.1: An overview of the CMS detector. The ECAL is displayed in turquoise immediately surrounding the Silicon Tracker. The person in the image is approximately 2.0 m tall[8].

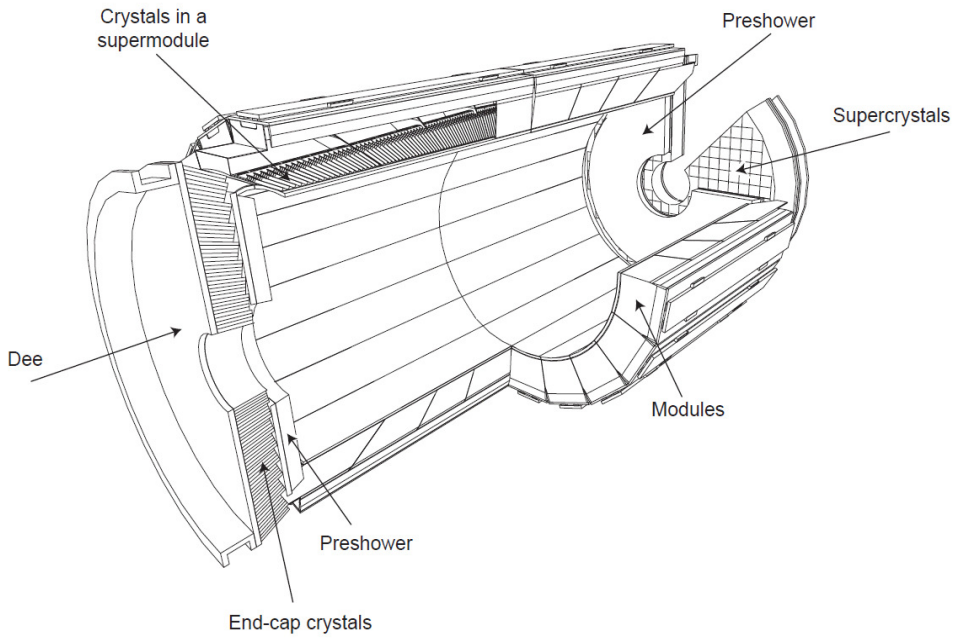

FIGURE 2.2: Layout of the CMS ECAL. The rows visible in the barrel are crystal scintillator *supermodules*. All of the 36 supermodules on the ECAL barrel contains 4 modules each with $400 - 500$ scintillating crystals. This results in the $61,200$ crystal scintillators in ECAL[7].

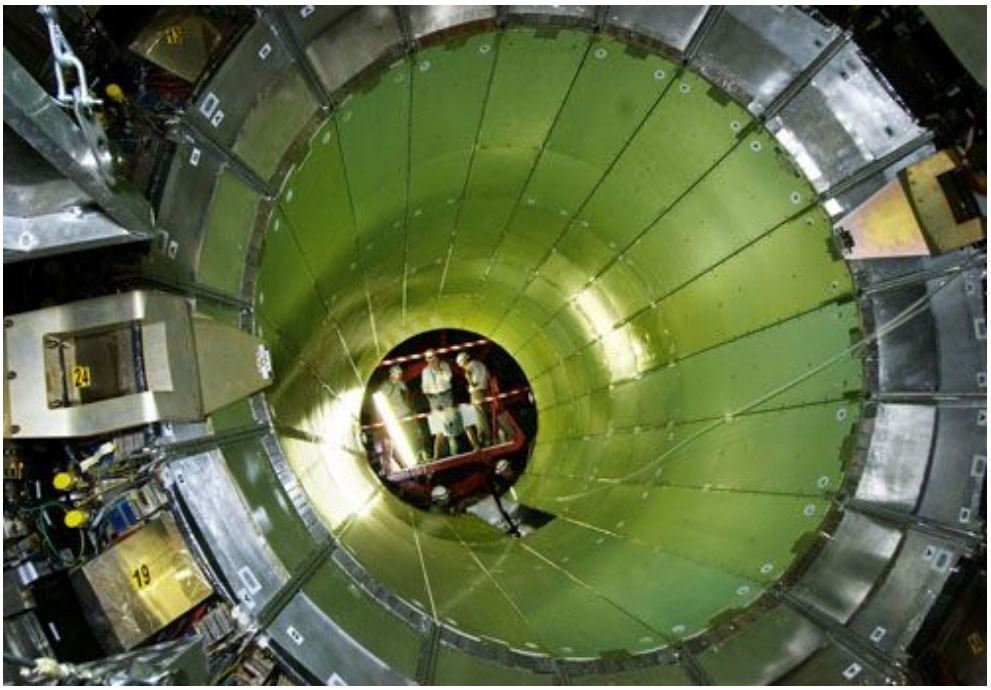

FIGURE 2.3: The CMS barrel ECAL under construction[8].

Information about electrons and photons measured by the ECAL is obtained by the measurement of scintillation light. This scintillation light is produced via the interaction of photons and electrons with crystal scintillators installed at the ECAL. When a photon or electron produced at the interaction point passes through the tracker, it is encountered by these scintillators. Through collision with these scintillators an *electromagnetic shower* consisting of light and other electromagnetic particles, is produced. This electromagnetic shower spreads to several neighbouring crystals and triggers other, less energetic electromagnetic showers. The energy of the components of the electromagnetic showers is eventually converted to photons through the scintillation process. Light produced in each crystal then travels down that crystal and is collected and measured by photodetectors[7].

2.1.1 Lead Tungstate Crystals

Within the barrel ECAL there are $61,200$ high density Lead-Tungstate ($PbWO_4$) crystal scintillators. These are 23 cm long and have a tapered shape. These crystals have a pseudo-projective geometry towards the interaction point[1]. The front of the crystals is 2.2 cm wide which uniformly extends to 2.6 cm at the rear face[7]. The Moliére radius[2] is 2.2 cm which results in an average 90% of electromagnetic shower being contained

[1]The narrow end faces in the direction of the interaction point without allowing any accessible gaps between the crystals.

[2]This is the radius of the cylinder containing on average 90% of the electromagnetic shower which is produced and is travelling along the scintillator.

within each crystal. The crystals[3] were constructed for CMS specifically due to their good radiation tolerance, small radiation length[4] ($X_0 = 0.89\ cm$) and fast response where 80% of the light is emitted within 25 ns [7]. This is comparable to the mean time between LHC collisions, thus reducing the probability of overlapping signals in the same crystal.

2.1.2 Avalanche Photo Diodes

The scintillation light produced by the crystals is detected by Avalanche Photo Diodes (APDs). Two of these devices are glued to the back of each crystal (Figure 2.4). These were chosen due to their good radiation tolerance, high quantum efficiency[5], their stability, as well as their ability to operate under the influence of the CMS 3.8 T magnetic field[7].

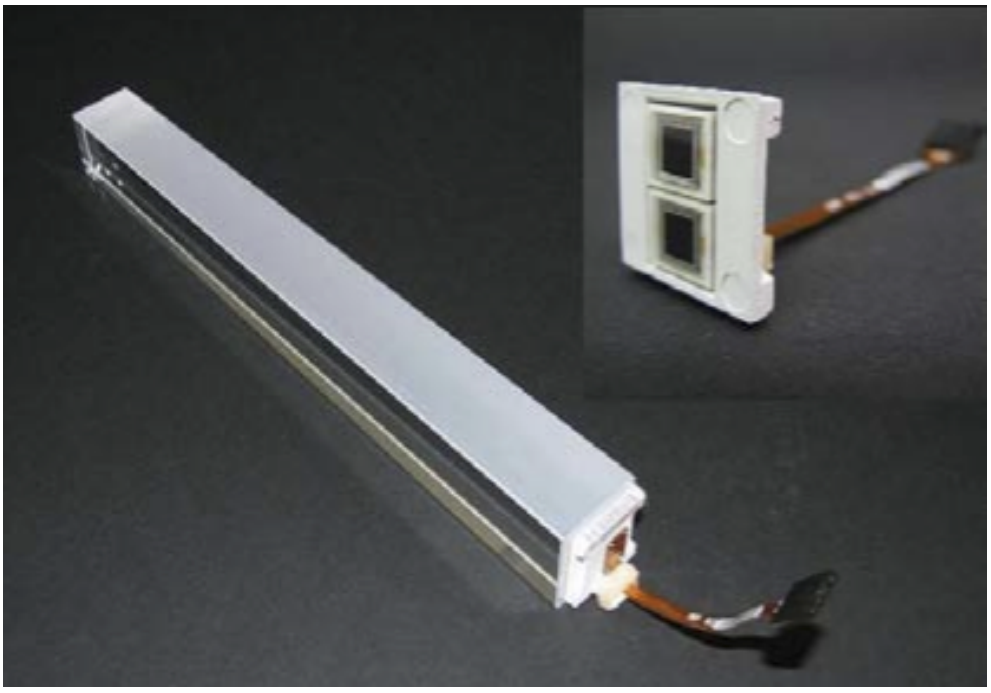

FIGURE 2.4: A Lead Tungstate crystal from the barrel ECAL with two APDs glued at the base. The top right corner depicts the APDs front face prior to being glued to the crystal[8].)

The operation of APDs relies on *avalanche multiplication* for measuring signals above a certain energy threshold. Avalanche multiplication occurs when a photon of sufficient

[3]These relatively small transparent crystals are deceptively heavy ($\rho = 8.28\ g/cm^3$) weighing at around 1 kg each. I, like many others, almost dropped the £1000 scintillator sample when holding it for the first time. Such accidents are likely not covered by our respective institutes and so appropriate care is advised.

[4]This is the distance a high energy particle needs to travel in order to lose $\frac{1}{e}$ of its energy through interaction with the material [7]

[5]This a measure of how well optical photons absorbed and used in the generation of primary charge carriers.

energy enters the $\approx 50\ \mu A$ silicon PN junction within the APD and ionises one of the lattice atoms. Due to the tuning of the reverse bias applied to the P-N junction, the resulting free electron has enough energy to ionise another atom within the lattice and so on, with all these electron/hole pairs now acting as charge carriers across the $P - N$ junction. The result of this process is the amplification of the signal received by the APD which operates with a gain of 50[9] in CMS.

Finally, it should be mentioned that the the front face of the APDs are covered with a protective epoxy coating which is on average 400 μA thick. This layer was included to act as a stabiliser for the two APDs attached to their mount which was then glued to the crystals. The cause of anomalous signals in the barrel ECAL is related to the presence of this epoxy layer[16]. This will be expanded upon in the next chapter.

2.2 The CMS trigger

The LHC is designed to provide $p - p$ collisions every 25 ns. This 40 MHz collision rate produces more data that can possibly be stored permanently. Many of the events at the LHC are not interesting from a physics perspective and must be filtered out[10]. The rate is reduced from 40 MHz to about 1 KHz by a real-time event selection system referred to as the *trigger*. This trigger has 2 main stages: The Level-1 trigger (L1) and the High-Level Trigger (HLT). The sequence of the event selection process is summarised in Figure 2.5.

These bandwidth limits exist due to limitations in the installed on-detector electronic components, the maximum practical data transfer rate from the detector, and the available real-time computing and storage resources[10].

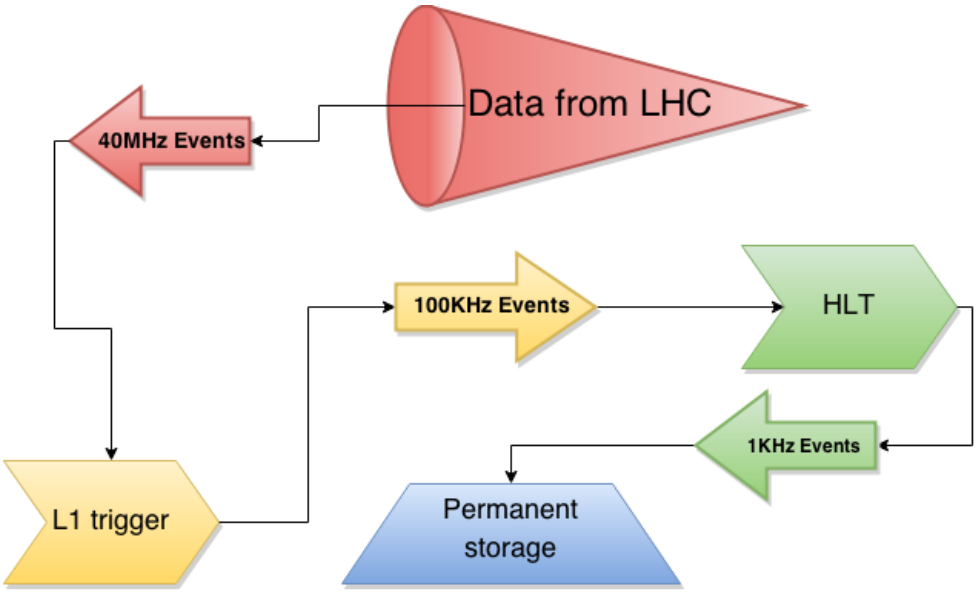

FIGURE 2.5: This diagram summarises the event rate reduction at each stage of the trigger in CMS.

2.2.1 Triggering on $e\gamma$ signals

The pattern of energy deposited in neighbouring ECAL crystals is used to trigger on electrons and photons in CMS. The energy associated with an electromagnetic shower is calculated by summing the energy in a 5×5 crystal array (or tower) with the largest energy deposit in one of the four adjacent towers (see Figure 2.6). Since an electron or photon deposits energy in a narrow region compared to a jet, an additional requirement is that 90% of the energy in the central tower be within 2 adjacent strips of 1×5 crystals.

Finally, since electrons and photons generally do not pass through to the HCAL, the ratio of the HCAL to ECAL energies in the same direction must be less than 5%. If all these conditions are met, and the ECAL energy is greater than a set threshold, the event is triggered by L1 and passed on to the HLT[11].

2.2.2 Triggering on spikes

It has been observed in LHC data that spike production is linearly proportional to the collision rate[6] and logarithmically proportional to the centre-of-mass energy (see Figure 2.7)[12]. Since spikes are isolated high energy signals in the ECAL and do not have any signature in the HCAL, they often satisfy the L1 $e\gamma$ trigger requirements[11]. Due to the limits imposed on the trigger and because their rates increase with luminosity, spikes

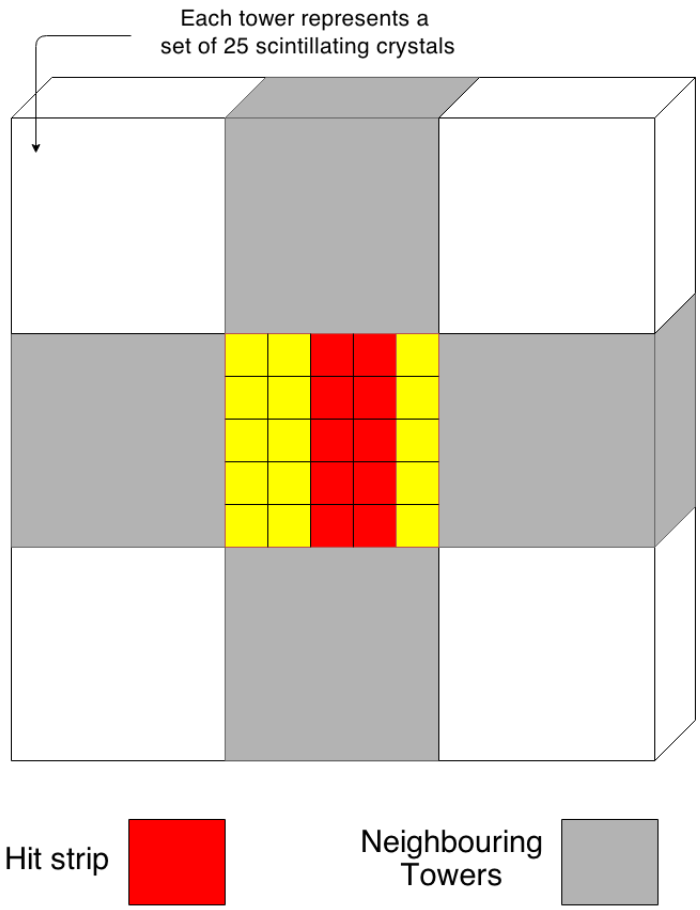

FIGURE 2.6: Selection of electrons and photons by the Level-1 trigger. When a central tower (set of 5×5 crystals) is flagged as having an energy above a certain threshold while its 4 neighbouring towers have an energy below the threshold, the trigger checks the energy distribution between individual crystal strips (in red and yellow) within the central tower. If the energy is distributed such that 90% is located in any two adjacent strips (shown in red), the deposit is considered to be $e\gamma$-like. This example demonstrates the signature of an electromagnetic shower due to a photon or an electron.

will affect the efficiency for selecting good $e\gamma$ signals. In addition, for future running of the LHC at higher luminosity (HL-LHC)[13], an even larger proportion of L1 $e\gamma$ triggers will be due to spikes. This is caused by three factors: the increase in luminosity (about a factor of 5), the increased centre-of-mass energy (about a factor of 1.4 due to logarithmic scaling) and the increased pileup[6](about a factor of 7 due to linear scaling). Given these much larger spike rates, they will dominate the available trigger bandwidth if the are not effectively mitigated (see Table 2.1).

[6]Since the LHC operates at such high luminosities, each time a collision takes place (beams cross), several simultaneous interactions between protons occur. The average number of these interactions per collision is referred to as *pileup* (PU). In LHC conditions in 2012, a pileup of 20 interactions was observed in CMS[10].

C.o.M energy (TeV)	Spikes per triggered event	Spike rate	
		Prior to L1	Prior to HLT
0.9 (measured, PU=0)	$(1.666 \pm 0.089) \times 10^{-3}$	$\approx$ 66 KHz	$\approx$ 2.6 KHz
7 (measured, PU=0[7])	$(2.697 \pm 0.005) \times 10^{-3}$	$\approx$ 107 KHz	$\approx$ 4.3 KHz
14 (predicted, PU=0)	$(3.665 \pm 0.007) \times 10^{-3}$	$\approx$ 147 KHz	$\approx$ 5.8 KHz
14 (predicted, PU=140)	$\mathbf{(5.13 \pm 0.01) \times 10^{-1}}$	**$\approx$ 20.5 MHz**	**$\approx$ 821 KHz**

TABLE 2.1: Summary of the long term effects of spikes on the trigger system. The 40 MHz event rate is a result of the 25 ns sampling frequency assumed for collisions at the LHC. The spikes scale logarithmically with energy and linearly with pile up. Calculations here are based on signals with an energy above 3 GeV. **The bold row** represents the predicted spike rate at a pile up of 140 expected at the High Luminosity LHC in the future[13]. The current spike rejection rate after the Level-1 trigger is assumed to be 96% based on previous studies [6, 12, 14].

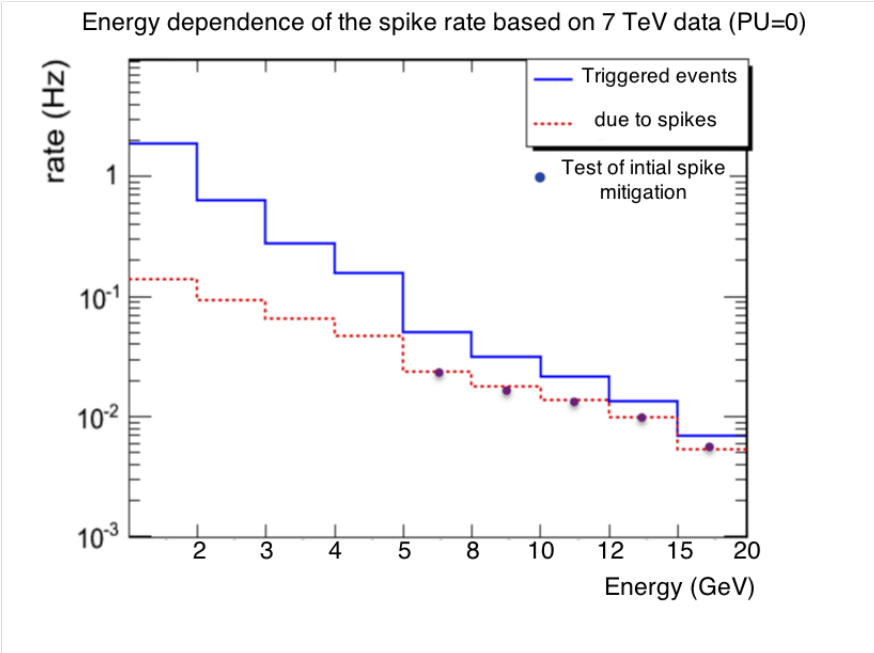

FIGURE 2.7: The total rate of electromagnetic triggers at Level 1 (solid line) that are due to spikes (dashed line) as a function of transverse energy. The data used was recorded during the early stages of 7 TeV data taking. The data points are derived from the mitigation rates of an already existing spike mitigation algorithm scaled to the luminosity of the earlier data[12].

Data from Table 2.1 suggests that even with the current mitigation algorithms (Chapter 4), the rates at the HLT are still quite high and will greatly reduce its efficiency for runs with higher pile up in the future.

This loss in trigger efficiency will lead to a proportionate loss in useful physics data. For example, the number of photons detected from $Higgs \rightarrow \gamma\gamma$ decays will be reduced proportionately and so would require a correspondingly longer running time of the LHC to gather enough events to reach accuracies that are required for meaningful statements regarding the properties of the Higgs. This is also true for $W^{\pm}$ bosons which decay

with end products of electrons or photons. The same argument is valid for any and all interactions that contain end products involving electrons or photons.

The presences of spikes also induces large biases in reconstructing the energies of electromagnetic events. Since a spike represents an anomalous large energy deposit, it will also result in large missing energy in reconstructed CMS events thus compromising many searches for physics beyond the Standard Model.

Finally, without any spike mitigation techniques, the energy threshold for $e\gamma$ triggers will need to be significantly increased way beyond what is acceptable to record electrons and photons with thresholds around $20 - 30$ GeV.

For the future, the current spike mitigation algorithms need to be improved and new more rigorous mitigation techniques need to be developed. These would ideally be implemented in L1 and the HLT.

Ahoy! Follow me for spikes!

Dave Cockerill, *Paraphrasing the author*

3

Properties of spike signals

The development of spike mitigating algorithms depends on understanding the origin and properties of these signals. Many studies have been performed on the characteristics of spikes in CMS data since their initial observation in 2009[6, 15, 16]. They are understood to be produced when charged particles produced in LHC collisions, directly ionise the APDs. Spikes have also been recreated in laboratory test of APDs and hadron test beams, further supporting this hypothesis[16].

APDs in the ECAL barrel have an epoxy coating $\approx 400\ \mu m$ thick. Within the APD itself there is a 50 μm thick layer of silicon acting as its PN junction. During $p-p$ collisions many neutrons and charged hadrons are produced. Since the epoxy is 8 times as thick as the silicon within the APD, direct ionisation of the epoxy by charged hadrons is common[1]. This results in a proton becoming dislodged from the epoxy lattice. Once a charged hadron, usually[2] a proton resulting from $n-p$ scattering within the epoxy, reaches the APD active silicon layer, it ionises the silicon. The resulting deposited energy then triggers the avalanche process within the APD. ECAL however, is calibrated to receive $e\gamma$ only *scintillation light* resulting from electromagnetic showers. Once it receives

[1]The cross section for $n-p$ scattering for neutrons with a few MeV of energy is on the order of one barn[16].

[2]Very infrequently charged $\pi^{\pm}$ particles undergo minimal scintillation within the crystals before reaching the APD active layer.

the large signal resulting from the heavily ionising hadronic interaction, it registers an anomalously large energy deposit. Figure 3.1 shows a diagram of this process.

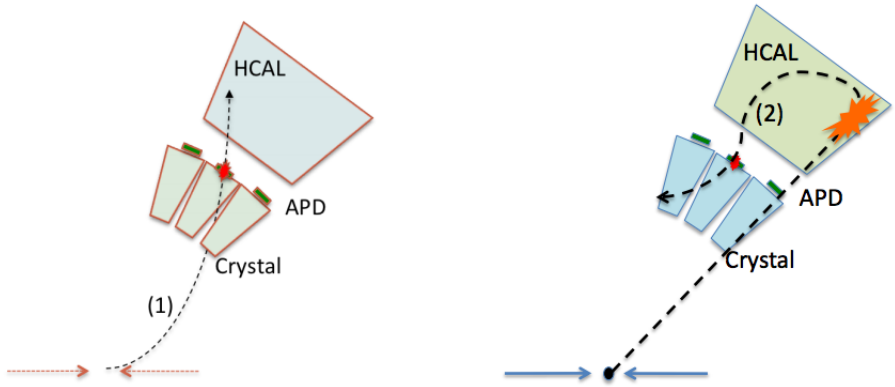

FIGURE 3.1: *Left:* A charged hadron heavily ionising the silicon layer within the APD. *Right:* A charged hadron being produced in the HCAL and ionising the APD from behind[17].

In addition to the spike observations in CMS and in laboratory tests, Monte Carlo simulations were developed that directly recorded the energies deposited in the APD active volumes. Spikes were also observed in these simulations, showing good agreement with CMS data and further cementing the theory that spikes originate within the APDs.

Spikes almost[3] always occur in a single APD channel as discussed. In addition, unlike $e\gamma$ particles, spikes typically do not generate electromagnetic showers through interaction with the scintillators. This results in a characteristic difference between the pulse shapes of $e\gamma$ signals and spikes. These differences between spikes and signals resulting from $e\gamma$ interactions must be exploited to obtain the best spike rejection efficiency. The remainder of this chapter will discuss these differences in more detail.

3.1 Energy topology

Typical electromagnetic showers resulting from scintillation light have a well-defined spread of energy between adjacent crystals with $\approx 80\%$ of the energy being deposited in one central crystal and the remaining 20% in the four nearest neighbours. Spikes on the other hand are almost always contained within a single channel. To utilise this property the *Swiss-Cross* variable was introduced (Figure 3.2).

The definition of the Swiss-Cross is shown in Figure 3.2. Here E_1 is the energy deposited in the central crystal channel. E_4 is the sum of the energy deposited in its four adjacent crystal channels. Spikes will have a Swiss-Cross value close to 1 due to E_4 being small.

[3]It is possible for spikes to occur in two or more adjacent APD channels, however, this is unlikely given the number of spikes per acceptable events and the number of APD channels in ECAL.

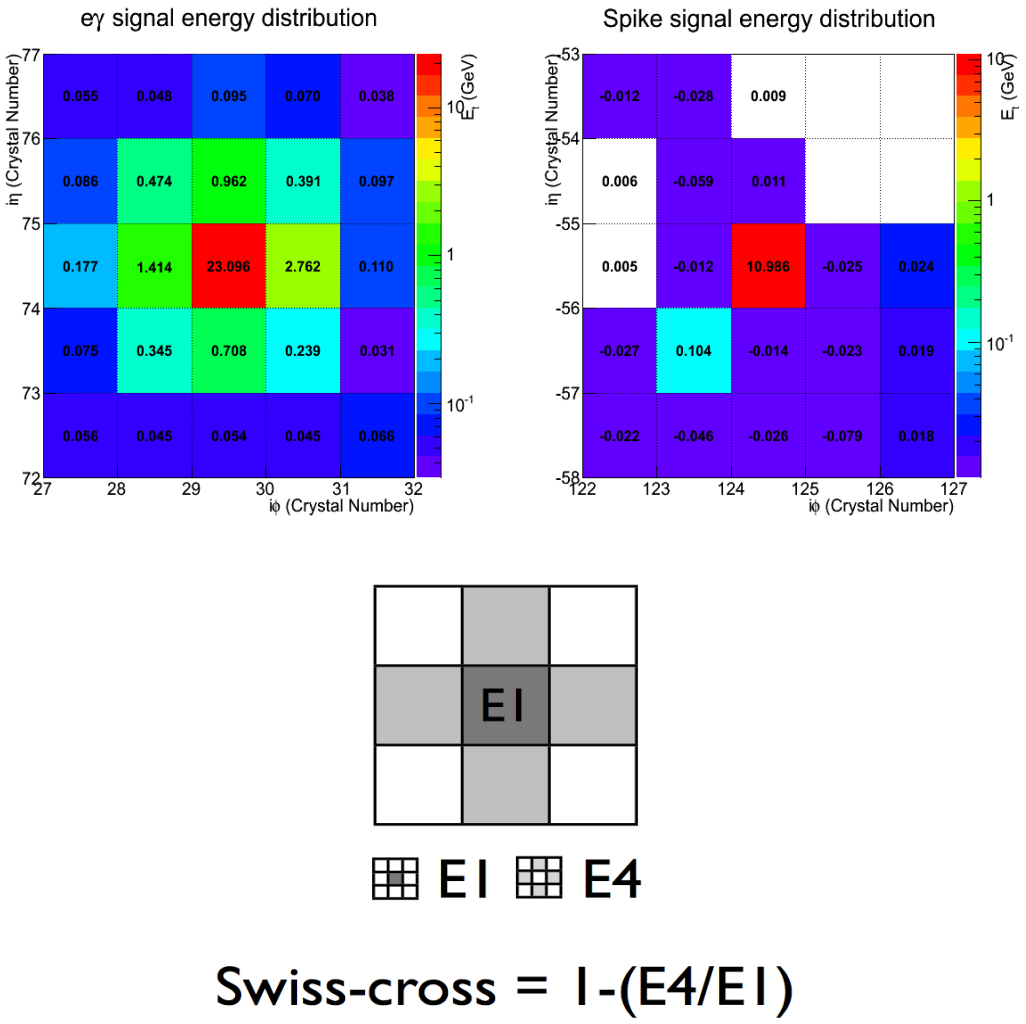

FIGURE 3.2: *Left:* The energy deposition per crystal of a 23 GeV $e\gamma$ signal. *Right:* The energy deposition per crystal of an 11 GeV spike. *Bottom:* The definition of the Swiss-Cross variable. Note that the negative energy readings in the top plot are due to fluctuating noise levels in the APDs.

The Swiss-Cross value for electromagnetic showers will be generally < 0.9 due to the additional energy from the electromagnetic shower in the neighbouring channels (E_4). This variable can, therefore, be used for spike mitigation.

3.2 Pulse shape

In ECAL the analogue signal from each channel (described in more detail in Chapter 6) is currently sampled at 40 MHz (once every 25 ns) with 10 samples recorded by the system per event.

Spike signal generation does not involve the crystal scintillation process and so, their pulse shapes differ from those of typical electromagnetic showers. Average pulse shapes of spikes and $e\gamma$ signals are shown in Figure 3.3. The average spike signal rises to its peak $\approx$ 10 ns earlier[4] than that of an electromagnetic shower. This difference in pulse shape can be used to identify and reject spikes in CMS.

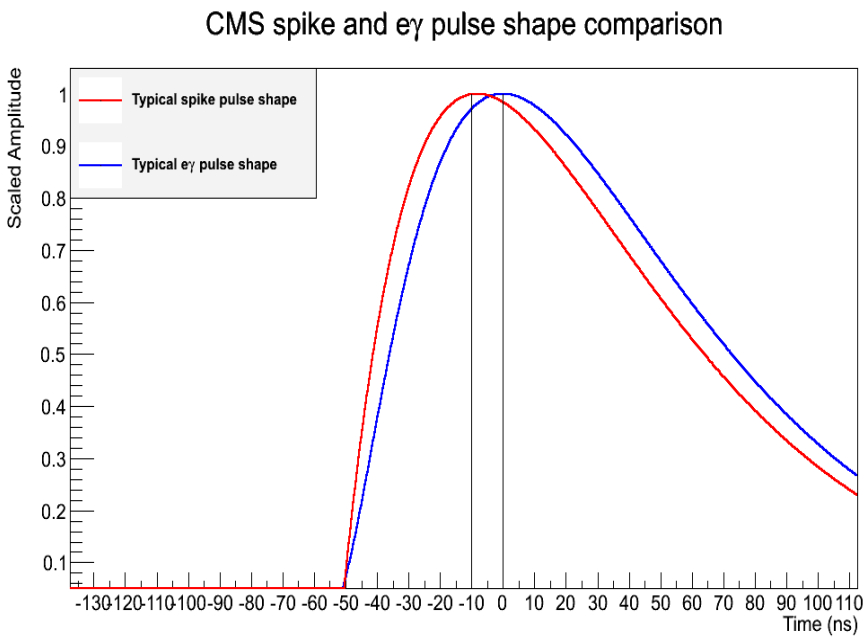

FIGURE 3.3: Typical spike and $e\gamma$ pulse shapes. Due to the faster rise time of the spike pulse shape, even though both the $e\gamma$ and spike pulse shapes arrive at the same time, the time of the peak of the spike pulse is at -10 ns while the $e\gamma$ signal is correctly calibrated to 0 ns. These pulses are derived from CMS data.

3.3 Reconstructed time

The ECAL detector has excellent ($<$ 1 ns) time measurement capabilities, due to the fast response of the crystals, together with the precise measurement of the signal pulse shapes [18]. The arrival time of a particle impinging on the ECAL is computed by comparing the measured pulse shape with a reference obtained from an electron test beam[18]. A further correction is made to account for the time of flight of a photon or a relativistic electron produced at the interaction point in CMS, such that the average arrival time (referred to as the *reconstructed time*) is zero for all channels in the ECAL.

Because the spike pulse shape differs from that of an electromagnetic shower (faster rise time visible in Figure 3.3) the apparent arrival time generally appears early relative to an $e\gamma$ signal. For a spike produced promptly with the LHC collisions, the reconstructed

[4]The 10 ns scintillation time results from the properties of the $PbWO_4$ crystals which I had the opportunity to measure directly in test beam experiments conducted in September of 2014.

time will be ≈ 10 ns *early*. The origin of this 10 ns bias is the scintillation decay time in the crystals that is not present in the spike signals.

This apparent difference in arrival time can also be used to distinguish between spike and $e\gamma$ signals.

Don't believe everything you read on the internet.

Winston Churchill

4

Current spike mitigation

Since the origin of the spikes is intrinsic to the APDs, any permanent solution would require the full dismantling of the 36 barrel supermodules (each containing $1,700$ crystals) to perform a full replacement of the APDs or reworking of the APDs signals. This is a costly and very time consuming operation which cannot be accommodated in the upgrade schedule of CMS. In addition, it carries with it significant risks to the detector (Danger of breaking crystals when the APDs are removed). The combination of these factors, makes this option not feasible.

The current mitigation techniques used in CMS reject spikes by using the spike features described in the previous chapter, together with the functionality available in the existing on-detector ECAL readout electronics. There are two levels of spike mitigation used:

1. *Prior to the Level-1 trigger (Online):* These are methods which are placed before the Level-1 trigger and alleviate the risk of the *loss* of useful physics data.

2. *After the Level-1 trigger (Offline):* These are more complicated algorithms that are used at the HLT or in the offline reconstruction of data for physics analysis. Although these do not prevent the loss of useful bandwidth at L1, they do reduce the spike rates in datasets that are used for analysis.

4.1 Online spike mitigation

Since the Level-1 trigger information from the ECAL must be read out at 40 MHz, only very simple pulse reconstruction algorithms are possible. In particular, the use of detailed pulse shape differences, described in the previous chapter, cannot be used.

The current spike mitigating algorithm implemented at the Level-1 trigger is the strip Fine Grain Veto Bit (sFGVB). This uses a feature that exists in the FENIX chip used at the front-end electronics[1] currently installed in the ECAL supermodules[6]. By using topological information, the sFGVB algorithm searches for towers with *more* than one crystal in a strip above a configurable threshold, and only triggers CMS when this *shower-like* topology is observed. In Figure 4.1 the operation of this algorithm is detailed in response to an electromagnetic shower.

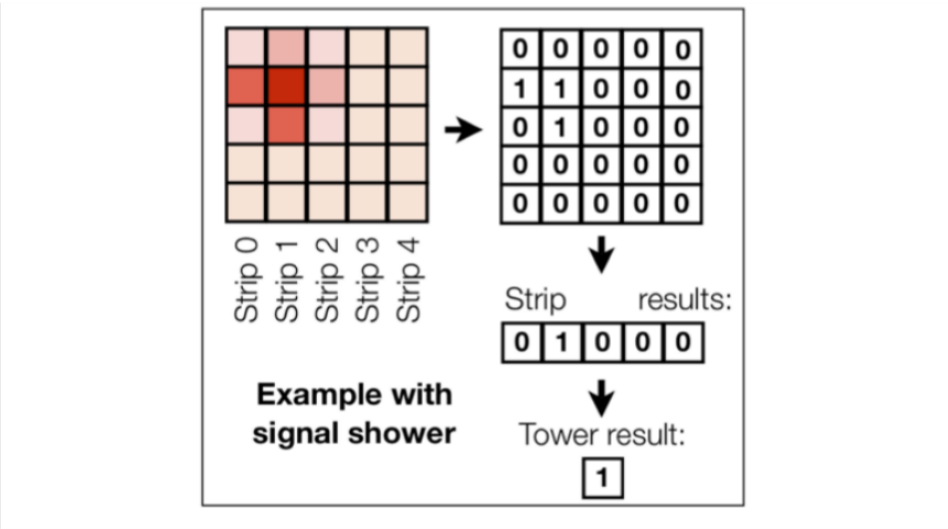

FIGURE 4.1: This plot demonstrates the function of the sFGVB algorithm. It shows how a shower or spike is flagged based on its energy topology. If the bit returns false (bit=0), the entire crystal tower is excluded from the trigger.

Once a tower (set of 5×5 crystals) is flagged as having an energy above a certain threshold (12 GeV in 2012), the sFGVB algorithm checks the energy deposition in each strip (a column of 5 adjacent crystals) of the tower and checks them against another threshold (350 MeV in 2012)[6]. If the energy in at least two channels of a 1×5 crystal strip is above this second threshold (350 GeV), a bit is set indicating that the strip is shower-like. Finally, the 5 bits resulting from the 5 strips are ORed together and the resulting single bit instructs whether the tower should be triggered upon or not. Given this algorithm, towers with more than 12 GeV of energy containing only isolated energy deposits above 350 GeV will not trigger CMS.

[1] These are the electronic circuitry behind the crystal supermodules.

The sFGVB has been measured to be $\gtrapprox$ 95% efficient in rejecting spikes with a $\lessapprox$ 2% probability of excluding $e\gamma$ signals[15]. However, it cannot eliminate those spikes that occur within a tower where an $e\gamma$ event has been recorded. Furthermore, $e\gamma$ signals occurring near the tower borders can be mistaken for spikes due to their apparent isolation in the tower. This is also true for $e\gamma$ signals that have a lateral energy distribution below the required strip threshold. Assuming 25% of the energy of a typical electromagnetic shower is deposited evenly between each of the four adjacent crystal channels results in signals with less than 4.2 GeV being excluded from the trigger due to the sFGVB algorithm. At higher luminosities, with increased detector occupancy (due to pileup) and noise, the performance of the sFGVB will progressively degrade[19] and the algorithm will need to be improved.

4.2 Offline spike mitigation

4.2.1 The Swiss-Cross

The Swiss-Cross variable (Figure 3.2), which is too complex for implementation at the Level-1 trigger, is implemented at the HLT. This has the effect of flagging some of the spikes that were missed by the sFGVB. The usefulness of this variable in spike mitigation is illustrated in Figure 4.2. This shows the Swiss-Cross distribution for 2012 CMS data (left) and for a specially-generated Monte Carlo sample consisting purely of spikes (right). Here the peak at around Swiss-Cross = 0.75 in the left-hand plot is due to real $e\gamma$ signals where the energy is shared between multiple crystals. The peak on the right of this plot at Swiss-Cross = 1.0 is due to spikes, which is replicated by the dedicated spike Monte Carlo (right-hand plot). A cut on the Swiss-Cross variable of 0.9 (vertical line in the plots) rejects >98.5% of spikes with a negligible impact on the efficiency for selecting electrons and photons.

4.2.2 Reconstructed time

It was revealed in Chapter 3 (and Figure 3.3) that the reconstructed time of signal pulses can discriminate between spikes and $e\gamma$ signals due to the different pulse shapes between the two. This is illustrated in Figure 4.3, which shows the timing distribution for 2012 CMS data (left) and the spike-only Monte Carlo (right).

The left hand plot exhibits peaks at 0 ns and ±50 ns, due to $e\gamma$ showers produced during LHC collisions (in 2012 collisions occurred every 50 ns, indicated by the shaded regions of the plots). The vast majority of $e\gamma$ signals are measured within 3 ns of the collisions.

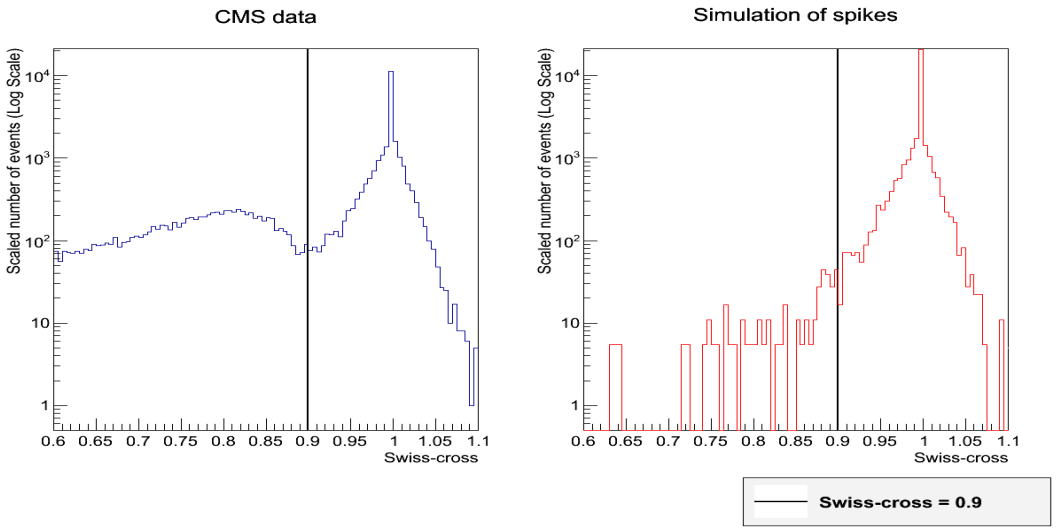

FIGURE 4.2: *Left:* The Swiss-Cross distribution of real CMS data *Right:* The Swiss-Cross distribution of Monte Carlo spikes.

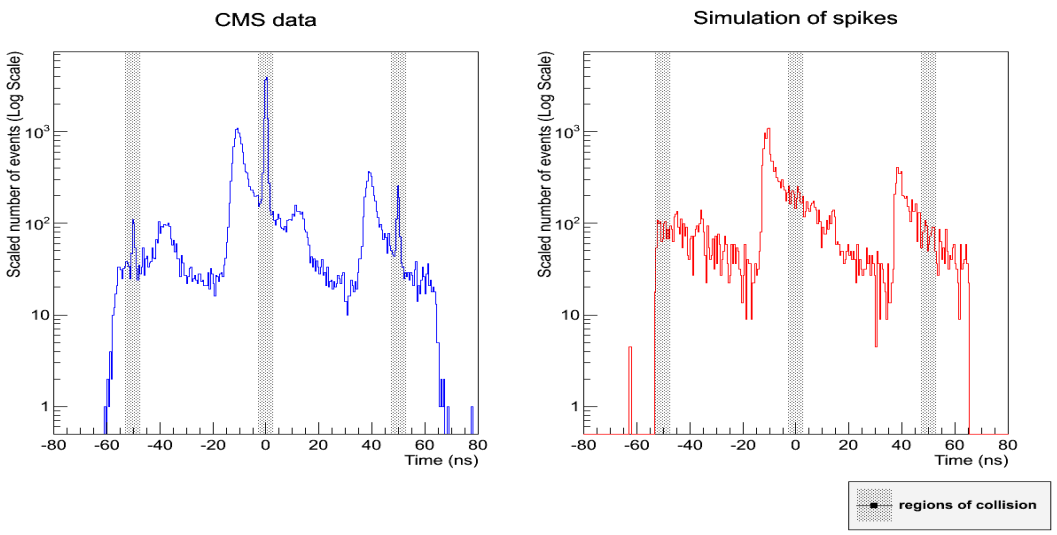

FIGURE 4.3: Distributions of reconstructed time for spikes and electromagnetic showers are plotted. *Left:* The reconstructed time distribution of real CMS data with shaded areas specifying time windows of LHC collisions. *Right:* The reconstructed time distribution of signals from a spike-only Monte Carlo simulation. This is from 2012 CMS data when collisions were occurring every 50 ns.

The spikes (right plot) on the other hand, are produced both inside and outside the collision windows. The peaks that occur 10 ns before the collisions are due to prompt spikes (remembering the 10 ns faster rise time of the spike pulse shapes). The spikes that occur elsewhere in this distribution are mostly due to neutrons produced in the collisions that drift around in the detector volume before undergoing $n-p$ scattering in the epoxy and producing a *delayed* spike.

Implementing a cut on the reconstructed time around the collisions timing windows eliminates a large fraction (>90%) of the spikes. This timing cut is only applied offline

and not at the HLT.

4.3 Uneffected spike regions

The mitigation techniques described thus far have allowed ECAL to meet its design requirements despite the presence of spikes[20]. As the LHC ramps up its energy and luminosity, the methods relying on the energy topology will gradually lose their efficiency due to higher pileup and noise.

In addition, the current spike mitigation methods in place do not mitigate those spikes which occur within the windows of collision and have a Swiss-Cross value smaller than 0.9. The two dimensional distribution of Swiss-Cross and reconstructed time for CMS events recorded in 2012 is illustrated in Figure 4.4.

On the top plot, the events with low Swiss-Cross values occurring every 50 ns are due to the occurrence of collisions and the presence of $e\gamma$ signals. The large number of events with Swiss-Cross values close to 1.0 across the entire region of time are caused by the long lived neutrons which exist in the volume of the detector before undergoing $n - p$ scattering in the epoxy. The concentration of events near $t = -10$ and 40 ns that extends to low Swiss-Cross values, indicate that some of the spikes are not isolated and so would fail the sFGVB algorithm at L1[2]. On the plot on the bottom, the regions in Swiss-Cross/reconstructed time space that have been effected by current mitigation methods are highlighted. It is visible that there are regions within the collision time windows where there is no mitigation being employed. This is problematic since it is precisely in those regions that spike mitigation is needed the most.

Finally, the pulse shape differences have not been directly exploited in mitigation methods employed thus far. The remainder of this document will concentrate on employing the pulse shape differences between spikes and $e\gamma$ signals directly, in the development of more advanced spike mitigation techniques.

[2]These are due to charged pions which undergo minimal scintillation within the crystals before ionising the APD protective epoxy.

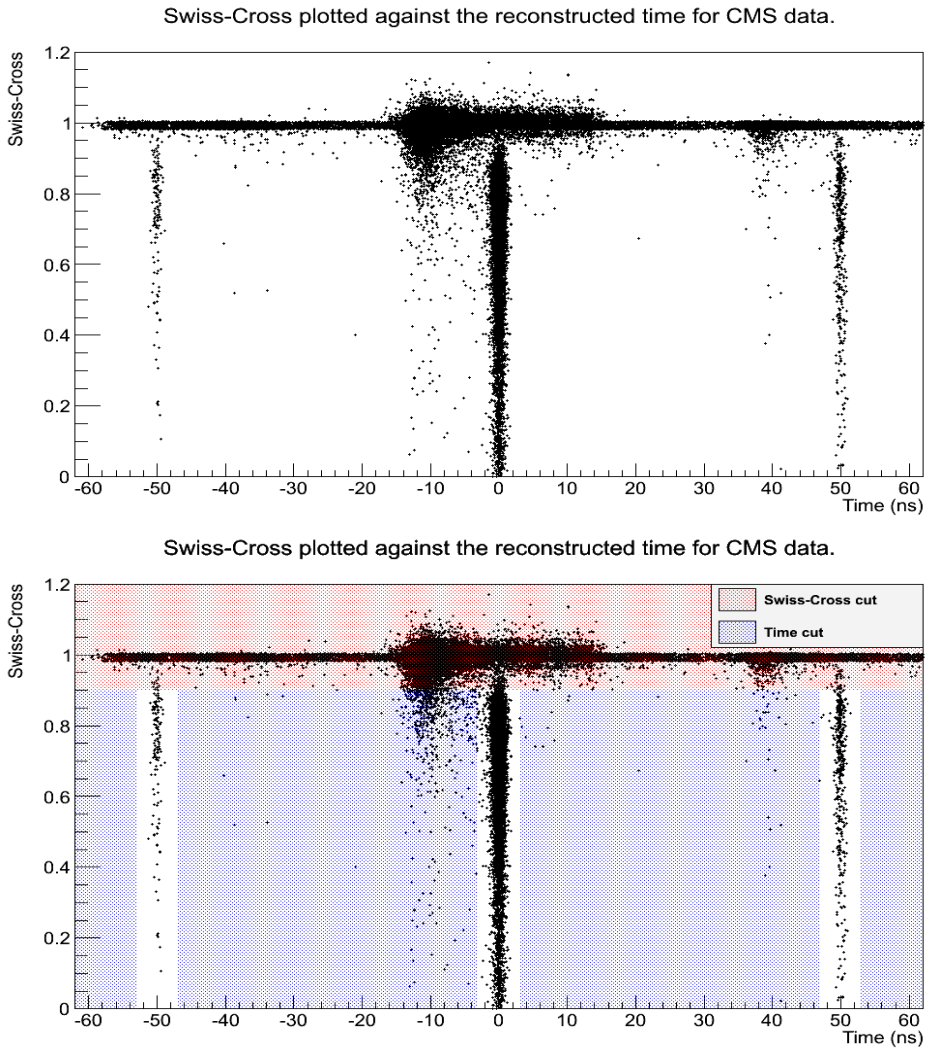

FIGURE 4.4: *Top:* The Swiss-Cross distribution of events from 2012 CMS data is plotted against their reconstructed time. *Bottom:* The cuts on the Swiss-Cross values and reconstructed time values which are currently in place in CMS are displayed. Note that the regions unaffected by either cut are when LHC collisions take place, and so, contain almost all $e\gamma$ events.

Ali Holmes and the Spikes of Baskerville.

Dave Cockerill, *Providing an accurate analogy*

5

Pulse shape analysis of 2012 data

The previous chapter described the existing spike mitigation methods, using the topological distribution of energy deposits, as well as the reconstructed time of the signal pulses. The latter has one disadvantage in that it cannot reject spikes that are accidentally *in-time* (such as those shown in Figure 4.3, right). Although the reconstructed time is an indirect measure of the difference in pulse shapes between spikes and $e\gamma$ showers (illustrated in Figure 3.3), the direct use of pulse shape information has not yet been exploited in CMS. This possibility will be investigated in the following chapters.

As mentioned earlier, the signal pulse shapes from the ECAL are digitised in 10 consecutive time samples, each of 25 ns duration. Average digitised pulse shapes from 2012 data are shown in Figure 5.1, for both spike and $e\gamma$ signals.

In this chapter, the performance of a statistical χ^2 test, already in place in the CMS event reconstruction, will be studied in its efficiency to discriminate between spike and $e\gamma$ pulse shapes.

5.1 The χ^2 test

The χ^2 statistic is a measure of the *goodness* of a particular fit when compared to measured experimental values. For a hypothesis with N different predicted values (t_i),

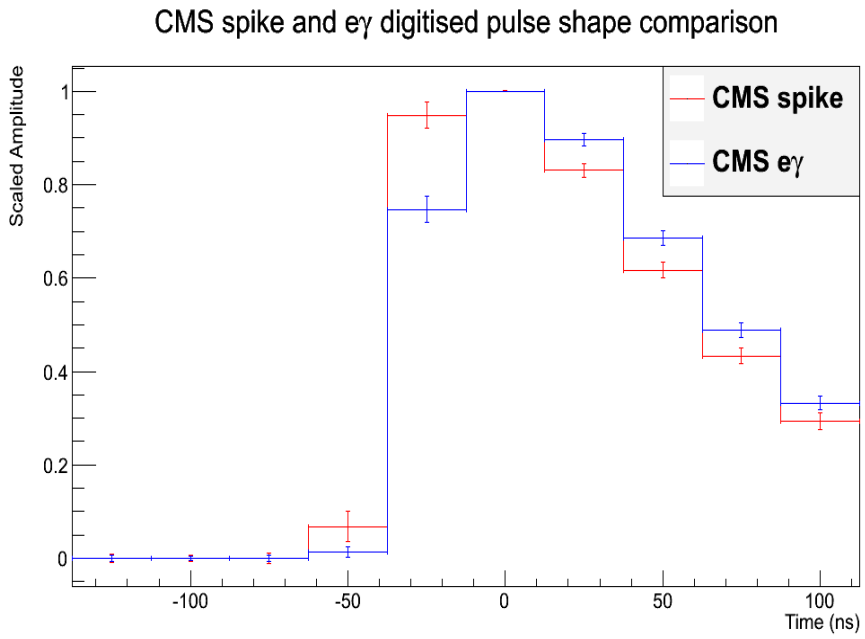

FIGURE 5.1: The digitised pulse shapes of $e\gamma$ signals and spikes are demonstrated here. These shapes are the average pulses of a large number of spikes and $e\gamma$ signals selected by compound Swiss-Cross and time cuts. The uncertainty for each bin is equivalent to one standard deviation.

each with a measured value of x_i, and a measured standard deviation of σ_i, the value of the χ^2 statistic[21] is defined by:

$$\chi^2 = \frac{1}{M}\sum_{i=1}^{N}\frac{(x_i - t_i)^2}{\sigma_i^2} \tag{5.1}$$

where M is the number of degrees of freedom of the measured system. In the case of digitised pulse shapes in ECAL, N represents the number of sampled points from the pulse shape and the x_i are values stored in each of the bins of the digitised pulse. The t_i are the corresponding reference values from a precise measurement of the $e\gamma$ pulse shape in a test beam. The standard deviation σ_i is the RMS value of the noise in each digitised channel due to the electronics in ECAL. Finally, since each bin is measured independently, and there exists no imposed constraint on the measurement of the digitised samples, the number of degrees of freedom (M) is equal to the number of sampled points (N) from the pulse shape. Therefore:

$$\chi^2 = \frac{1}{N}\sum_{i=1}^{N}\frac{(x_i - t_i)^2}{\sigma_i^2}\ , \qquad N = M \tag{5.2}$$

In this case, if the hypothesis (t_i) is accurate for the series of measurements x_i, all the terms in Equation 5.2 would be approximately equal to one and so:

$$\langle \chi^2 \rangle = 1 \tag{5.3}$$

Similarly, if the hypothesis is not accurate (which it is not in the case of spike pulses) the expected value of χ^2 will be greater than one.

5.2 The CMS χ^2

An implementation of the χ^2 test described in the previous section is already in place in the standard reconstruction of ECAL signal pulses in CMS. The first task in this study is to investigate the performance of this variable on 2012 data. Because of limited space in the data format used to store information from each channel, the χ^2 value is stored using 6 bits, with the following compressed scale:

$$\chi^2_{CMS} = 7(3 + \ln(\chi^2)) \tag{5.4}$$

This quantity is referred to as χ^2_{CMS} to distinguish it from the value of χ^2 defined in Equation 5.2. With this parametrisation, agreement with the the $e\gamma$ reference pulse shape ($\langle \chi^2 \rangle = 1$) would correspond to $\langle \chi^2_{CMS} \rangle = 21$.

In Figure 5.2, distributions of the χ^2_{CMS} are displayed from 2012 data. Spikes and $e\gamma$ signals have been selected using the following cuts:

- **For $e\gamma$ signals:** Swiss-Cross≤ 0.9 AND $|t_{rec} - t_{col}| \leq 3\ ns$.
- **For spike signals:** Swiss-Cross> 0.9 OR $|t_{rec} - t_{col}| > 3\ ns$.

where t_{rec} is the reconstructed time and $t_{col} = \{-50\text{ ns}, 0\text{ ns}, 50\text{ ns}\}$ are the corresponding times of LHC collisions. These cuts were displayed in Figure 4.4.

As expected, spike and $e\gamma$ signals peak at different values in their respective χ^2_{CMS} distributions. Despite peaking at a larger value, there are a significant number of spikes that have χ^2_{CMS} values that are close to those of the $e\gamma$ signals. This leakage will cause a decrease in both the spike rejection efficiency, as well as $e\gamma$ acceptance efficiency in any cuts made on the total χ^2_{CMS} distribution.

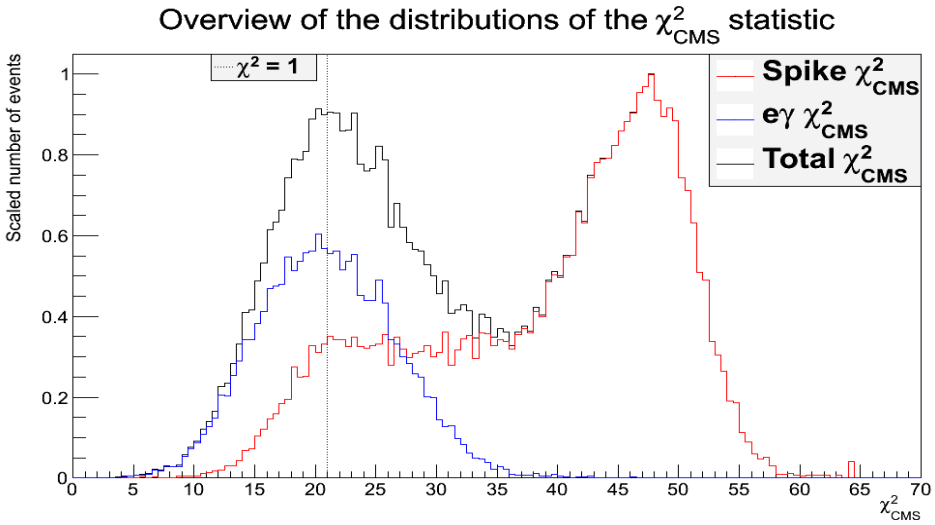

FIGURE 5.2: Distribution of χ^2_{CMS} for 2012 data. This displays the different χ^2_{CMS} distributions for $e\gamma$ and spike signals based on compound Swiss-Cross and time cuts. The total distribution is also displayed. Note that satisfactory agreement with the reference $e\gamma$ pulse shape is reached at $\langle\chi^2_{CMS}\rangle = 21$ (indicated by the vertical line).

The efficiency of a particular cut is calculated in the following way:

$$\text{Efficiency} = \frac{\text{Number of events passing the cut}}{\text{Total number of events}} \tag{5.5}$$

Here the denominator corresponds to the number of spikes or $e\gamma$ signals that pass the cuts listed earlier. The numerator corresponds to the number of spikes that are *above* a specific χ^2_{CMS} value, or the number of showers that are *below* that same cut. These are then termed the spike *rejection* efficiency and $e\gamma$ *acceptance* efficiency respectively. These quantities are computed for a range of χ^2_{CMS} values and the resulting 2D plot of spike rejection versus $e\gamma$ acceptance is shown in Figure 5.3.

The optimal cut (green point on the right hand plot) displays the value of $\chi^2_{CMS} = 28$ where the spike rejection and $e\gamma$ acceptance efficiencies are simultaneously maximised. At this optimal cut, the following efficiencies are achieved[1]:

$$\text{Spike rejection efficiency} = 0.7946 \pm 0.0006 \tag{5.6}$$

$$\text{e}\gamma\text{ acceptance efficiency} = 0.888 \pm 0.001 \tag{5.7}$$

[1]The uncertainties included here are due to the number of events that have passed each cut and are assumed to obey a Gaussian distribution the standard deviation of which is equal to the quoted uncertainties.

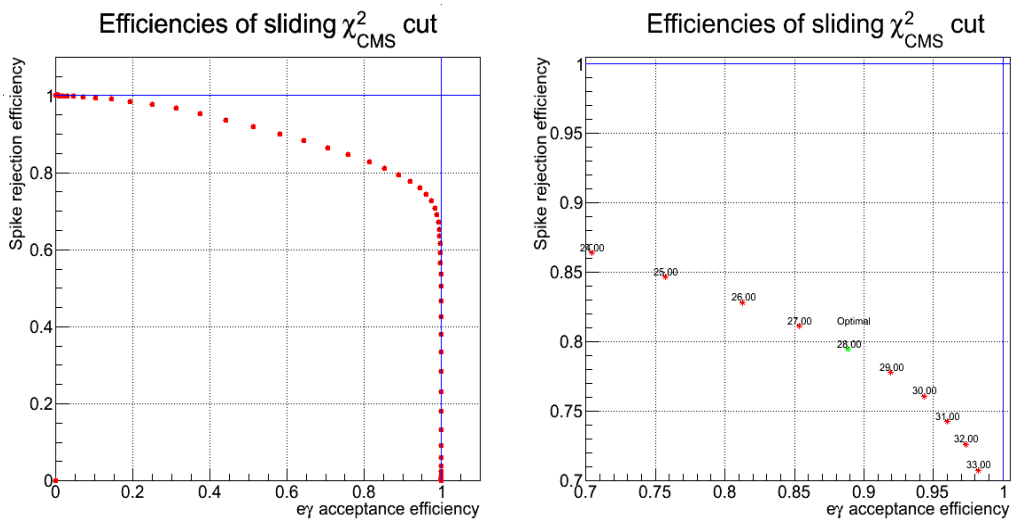

FIGURE 5.3: *Left:* Spike rejection efficiency plotted against $e\gamma$ acceptance efficiency for a range of cuts on the total χ^2_{CMS} distribution. The spike rejection efficiency steadily decreases as the value of the cut on the χ^2_{CMS} distribution increases. *Right:* A zoom of the plot on the left hand side. The optimal cut (in green) displays the value of $\chi^2_{CMS} = 28$.

These efficiencies are well below those achieved by current mitigation techniques employed (Chapter 4). Considering the clear difference between spike and $e\gamma$ digitised pulses (Figure 5.1), the low efficiency values obtained were surprising. The likely cause for this drop in efficiency was thought to be those spikes which had a χ^2_{CMS} value close to that of the $e\gamma$ signals. As a result the spike distribution in Figure 5.2 was investigated further.

5.3 The χ^2_{CMS} blind spot

Following a detailed investigation of the source of this inefficiency, the root cause was finally identified. The key to solving this puzzle was to plot χ^2_{CMS} and the resulting spike rejection efficiency as a *function* of the reconstructed time. This is when the unusual periodic behaviour illustrated in Figure 5.4 was observed.

The striking feature of the plots in Figure 5.4 is that this data was recorded in 2012 when 20 MHz collisions (every 50 ns) were taking place at the LHC. In other words, there are no $e\gamma$ signals occurring at t=±25 ns. However, the spike rejection efficiency drops every 25 ns implying the presence of $e\gamma$-like signals. This behaviour is problematic since the region where the efficiency of the χ^2_{CMS} cut is low coincides with the time of LHC collisions - which is precisely the region where high efficiency is desired.

An investigation into the source of this behaviour revealed insight to the cause of the periodicity. It was found that for a specific digitisation phase relative to the reconstructed

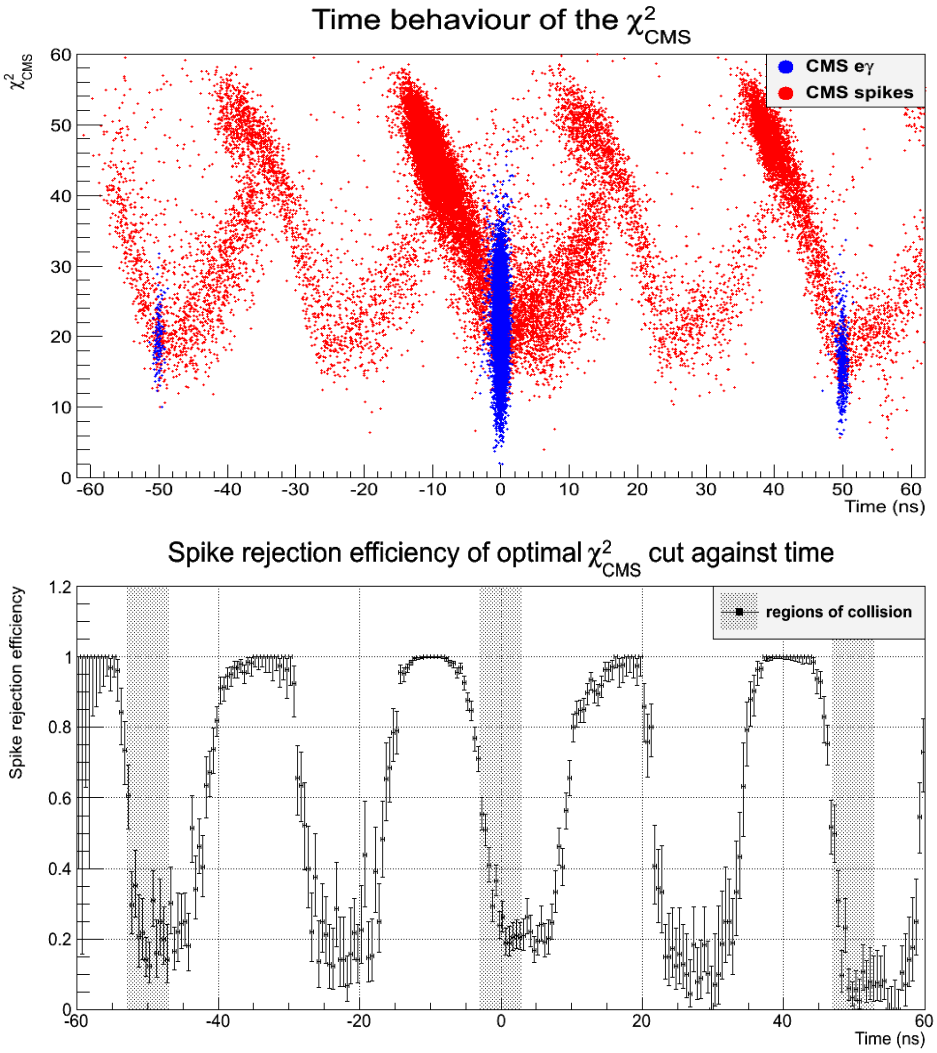

FIGURE 5.4: *Top:* The χ^2_{CMS} of 2012 data plotted against the reconstructed time of the events. Note the unusual periodic behaviour of the spike events. *Bottom:* The spike rejection efficiency behaves in an unexpected periodic manner which corresponds to the 25 ns LHC collision period.

time of signals, pulse shape data points from the spike signals lie on top of those from electromagnetic signals. This *blind spot*, a fundamental property of the 25 ns sampling frequency, means that the pulse shape of these spikes, reconstructed from the 10 existing data points, fits the template for electromagnetic signals, and so has a low value of χ^2. This situation is demonstrated in Figure 5.5.

One possible way to mitigate this is to shift the digitisation phase of ECAL, such that the blind spots occur outside the region of time where the LHC collisions occur. To evaluate the feasibility of this, along with other potential improvements, the development of a specialised pulse shape Monte Carlo simulation was pursued.

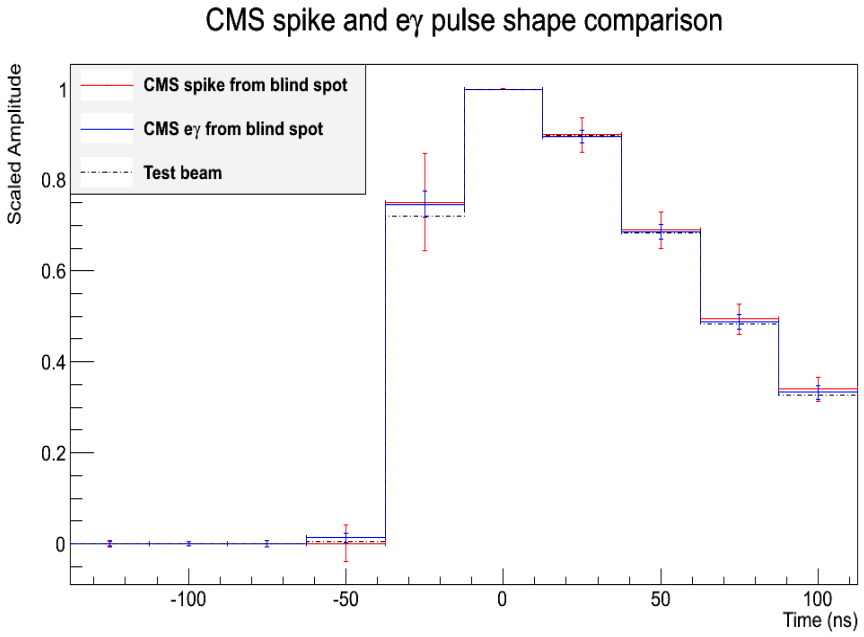

FIGURE 5.5: Average CMS spike and $e\gamma$ pulses within the χ^2_{CMS} blind spots, measured from CMS data are plotted. The shape of spike pulses from the blind spots fit the reference test beam as well as the shape of $e\gamma$ pulses.

The Uncertainty Principle will not help you now spikes.

The simulated Albert Einstein, *Star-Trek TNG S6.E26*

6

Development of a specialised pulse shape Monte Carlo simulation

A specialised pulse shape Monte Carlo simulation has been developed. This has been used to study the potential improvements in spike mitigation that can be achieved by modifying the parameters associated with the pulse digitisation process in ECAL. These results will be used to guide the requirements of the upgraded ECAL barrel front-end electronics, which will be installed in 2023 prior to running of the High Luminosity LHC (HL-LHC).

The development of a pulse shape Monte Carlo for both spikes and $e\gamma$ showers relies on the accurate simulation of the pulse digitisation process within ECAL. This process was briefly described in Chapter 3. Here it will be described in more detail so that all possible aspects of the digitisation process can be tuned in the investigation of pulse shape reliant spike mitigation techniques. The accuracy of this simulation is checked by attempting to reproduce the qualitative features of the data that are described in Chapter 5, including the blind spots in the χ^2_{CMS} variable observed in Figure 5.4.

The starting point in the digitisation process (Figure 6.1) is the arrival of an $e\gamma$ signal or a spike. This signal is then amplified to diminish the relative noise present. The analogue pulse is then convoluted with an electronic shaping function which has the effect of extending the pulse, thereby accentuating the existing features as well as reducing the

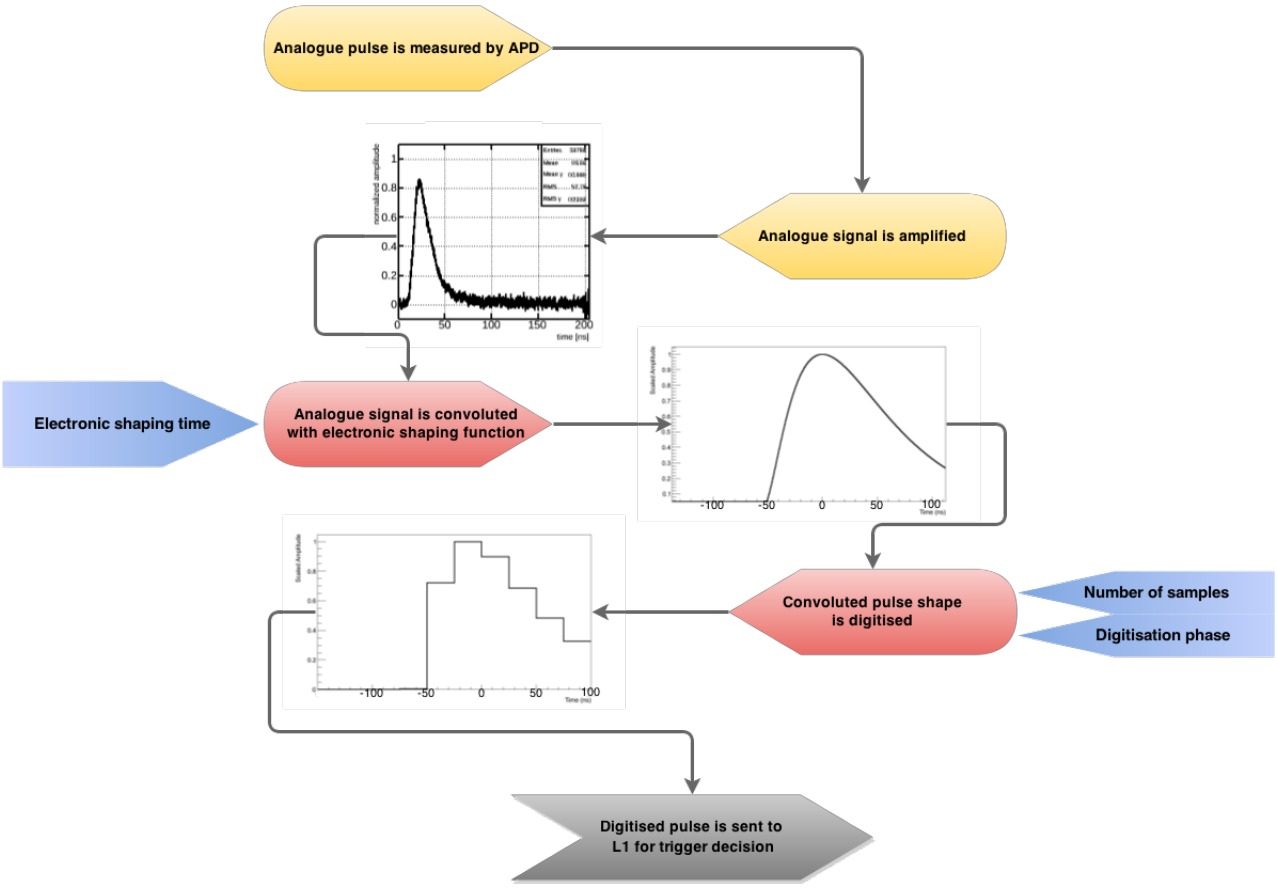

FIGURE 6.1: Summary of the digitisation process in ECAL. The stages in yellow are stages where alteration without a hardware upgrade is not possible. The red stages take input which can be changed without a significant upgrade in hardware. The input to these parts of the digitisation process is depicted in blue.

noise further. The electronic shaping function has a corresponding shaping time which can be altered to dictate the degree to which the pulse is extended. Finally, the readout digitises this convoluted shape with a set number of samples per pulse (10 samples currently). The readout phase that can be adjusted here. The sampling frequency is currently 40 MHz resulting in one sample every 25 ns. The digitised pulse shape is then sent to the Level-1 trigger where the decision of triggering on the signal is made[7]. The electronic shaping time, digitisation phase, and the number of samples are features which need to be explored and so require flexibility in the simulation.

6.1 Simulation of analogue pulse shapes

The simulation proceeds step by step, following the flow diagram shown in Figure 6.1. The first step involves the generation of the analogue pulse shape which will be convoluted with the electronic shaping function. To do this, the electronic shaping function, as well as the functional form of the expected analogue signal are required.

The electronic shaping function follows the design of the existing ECAL electronics, which uses a CR-RC[1] network[22]. The shaping function is described in Equation 6.1 where τ_e is the electronic shaping time.

$$f(t) = (\frac{t}{\tau_e})e^{-(\frac{t}{\tau_e})} \qquad \text{Electronic shaping function} \tag{6.1}$$

$$g(t) = (\frac{1}{\tau_s})e^{-(\frac{t}{\tau_s})} \qquad \text{Functional form of analogue } e\gamma \text{ pulse} \tag{6.2}$$

The analogue pulse shape for $e\gamma$ showers is assumed to follow an exponential time distribution[22], shown in Equation 6.2. This is governed by the decay time constant, τ_s, of the scintillation light from the $PbWO_4$ crystals. Here this constant is assumed to be $\tau_s = 10$ ns.

The convolution of these two functions simulates analogue $e\gamma$ pulse shapes in ECAL. Therefore, the functional form for a typical $e\gamma$ pulse is described by:

$$F_{e\gamma}(t) = (f * g) = \int_0^t f(s)g(t-s)ds \tag{6.3}$$

$$= (\frac{1}{\tau_e\tau_s})e^{-(\frac{t}{\tau_s})}\int_0^t s(e^{s(\frac{1}{\tau_s}-\frac{1}{\tau_e})})ds \tag{6.4}$$

$$= (\frac{1}{\tau_e\tau_s})e^{-(\frac{t}{\tau_s})}\int_0^t s(e^{\alpha s})ds \qquad , \qquad \alpha = \frac{1}{\tau_s} - \frac{1}{\tau_e} \tag{6.5}$$

$$= (\frac{1}{\tau_e\tau_s})e^{-(\frac{t}{\tau_s})}\big((\frac{1}{\alpha})te^{\alpha t} - \frac{1}{\alpha^2}(e^{\alpha t}-1)\big) \tag{6.6}$$

$$\Rightarrow F_{e\gamma}(t) = (\frac{1}{\alpha^2\tau_e\tau_s})e^{-(\frac{t}{\tau_s})}\big((\alpha t-1)e^{\alpha t}+1\big) \tag{6.7}$$

Spikes are caused by the direct ionisation of the APD silicon and, unlike electrons or photons, do not cause an electromagnetic shower within the crystal scintillators. Therefore, the avalanche process due to spikes in the APDs occurs much faster than those due to $e\gamma$ signals. As a result, the time evolution function of analogue spike signals is assumed to behave as a Dirac delta function which, when convoluted with the electronic shaping function, returns the electronic shaping function itself:

$$F_{spike}(t) = (f * \delta) = \int_0^t f(s)\delta(t-s)ds = f(t) \tag{6.8}$$

$$\Rightarrow F_{spike}(t) = (\frac{t}{\tau_e})e^{-(\frac{t}{\tau_e})} \tag{6.9}$$

[1]This is a circuit which shapes a periodic input and reduces its noise by having a low-pass filter followed by a high-pass filter.

In the current ECAL electronics, the shaping time τ_e is set to 43 ns. This choice was optimised to provide the best signal to noise ratio for the output, given the current noise levels in CMS. The analogue pulse shapes as currently set up in ECAL are simulated in Figure 6.2.

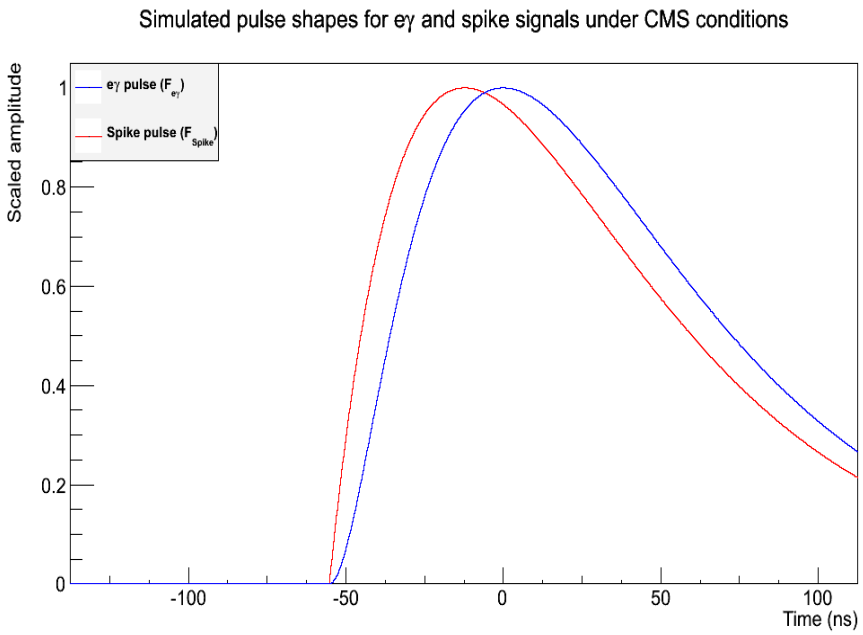

FIGURE 6.2: Simulated analogue pulse shapes for eγ showers and spikes.

In CMS currently, a +2 ns digitisation phase is applied. What this means in practice is that the signal pulses from $e\gamma$ showers do not reach their maxima in the middle of the 6th digitised sample (as they would if no phase was applied). Instead they reach their maxima 2 ns later. This was done in order to maximise the efficiency of the energy reconstruction algorithms used in the ECAL trigger, which are very sensitive to the precise value of the readout phase[23].

With this information, the digitised pulse shapes can be produced and treated as if they were CMS data.

6.2 Simulating the χ^2 behaviour of CMS

The χ^2 definition in Equation 5.2 requires three components:

1. *The digitised pulses:* These are obtained from the simulation using the method described above.

2. *A reference $e\gamma$ pulse:* Here this is assumed to be the functional form of $e\gamma$ pulses ($F_{e\gamma}$) described in Equation 6.7.

3. *Uncertainty in each bin of the digitised pulses:* Taken to be the level of electronic noise expected in CMS data.

In order to implement electronic noise in the simulation, the noise level is assumed to be:

$$\sigma_{43} = 60 \text{ MeV} \tag{6.10}$$

where σ_{43} is the current noise level in CMS appropriate for the existing electronic shaping time of $\tau_e = 43$ ns. This noise is added to each sample by randomly sampling a Gaussian distribution with $\sigma = 60$ MeV.

In order to provide a realistic simulation of spikes and electromagnetic showers in CMS, we also need to generate pulses according to the observed energy and timing distributions in data. This is particularly important as the relative contribution of noise is not equal for pulses of different energies. In addition, the relative phase of digitisation is dependent on the value of the reconstructed time. These distributions are obtained from 2012 data by identifying pure spike and $e\gamma$ samples using a combination of Swiss-Cross and timing cuts, and can be seen in Figure 6.3. This is followed by the production of large numbers of spikes and $e\gamma$ events by randomly sampling from the two different probability distributions discussed above.

A simulation of ≈ 37000 events using this method resulted in the χ^2 distribution displayed in Figure 6.4 for both $e\gamma$ and spike pulse shapes. Unlike CMS, here it is not necessary to apply any logarithmic scaling to the χ^2 value to save space, therefore the quantity plotted is indeed what is represented by Equation 5.2. The χ^2 distribution for $e\gamma$ showers has a mean of 1.0, which expected (Equation 5.3. The spike distribution contains two individual peaks, and is in qualitative agreement with Figure 5.2 from CMS data (note the different bin widths in the two plots).

One of the main goals of the simulation is to reproduce the periodic behaviour exhibited in the CMS χ^2 distribution for spikes (Figure 5.4). Figure 6.5, which uses simulated events, indeed demonstrates this periodic behaviour. From this plot is is clear that the blind spots are replicated by this pulse shape Monte Carlo, confirming its accuracy. By including the current digitisation phase of 2 ns, the blind spot appears in almost exactly the same place as in Figure 5.4.

Finally, the spike rejection and $e\gamma$ acceptance efficiencies of these simulated events were calculated (Figure 6.6). This plot was produced using the same method used to produce Figure 5.3 and described in Chapter 5. Immediately apparent is that the efficiencies in

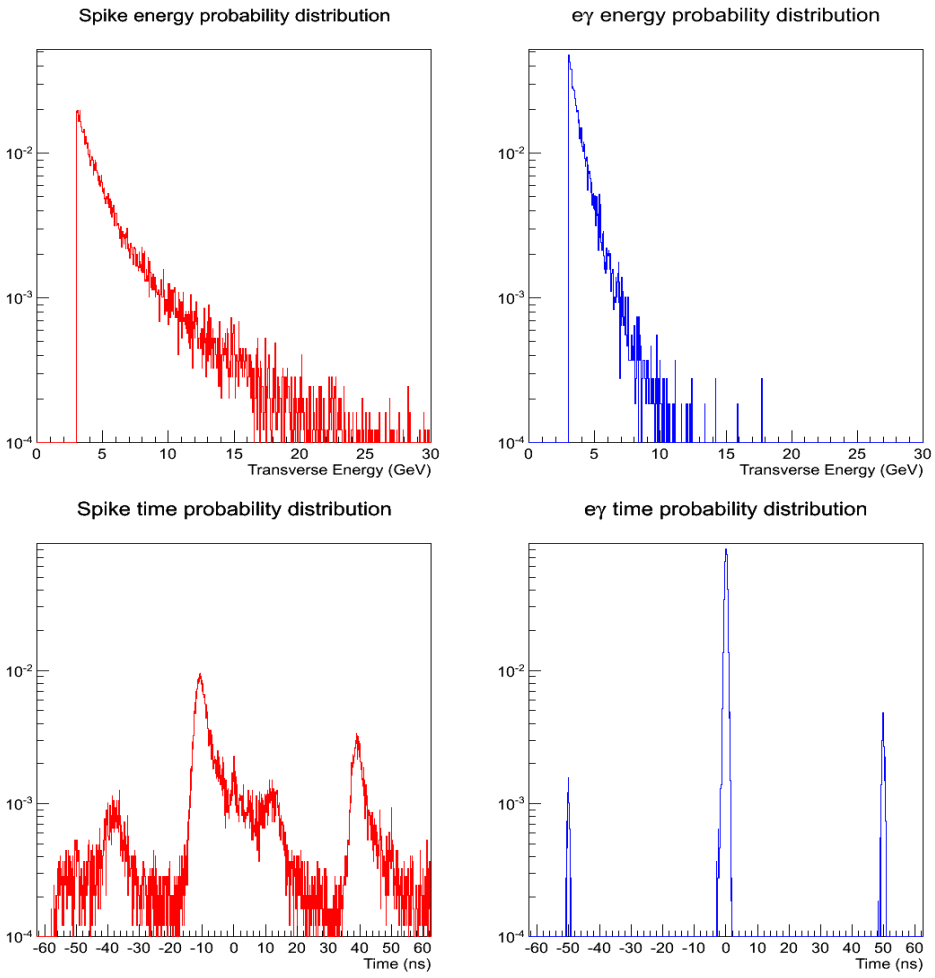

FIGURE 6.3: *Top:* The probability distribution functions for the reconstructed energy of both spikes and $e\gamma$ signals is displayed. Note that as expected, the spikes have a larger contribution to high energy signals. *Bottom:* the probability distribution functions of reconstructed time for spikes and $e\gamma$ signals are displayed.

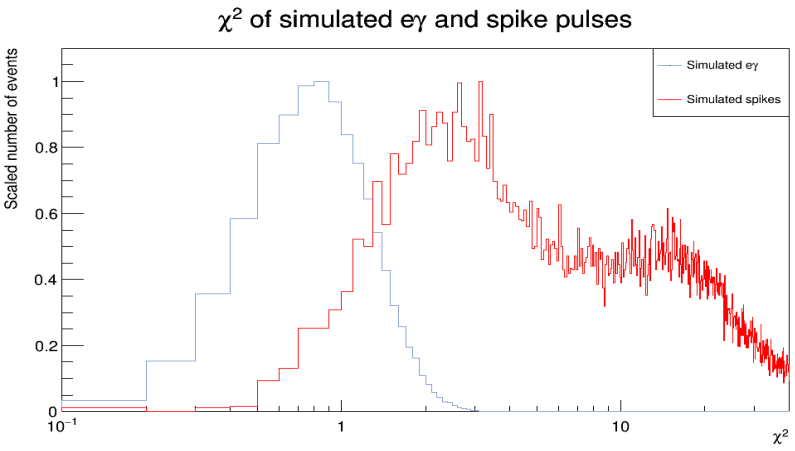

FIGURE 6.4: The distribution of the χ^2 for simulated $e\gamma$ and spike pulses. As in CMS, there exists a definite leakage of spike events into the $e\gamma$ distribution. Note that the horizontal axis is in logarithmic units to render the plot comparable to the CMS distributions (Figure 5.2) which contain the CMS parametrisation (Equation 5.4).

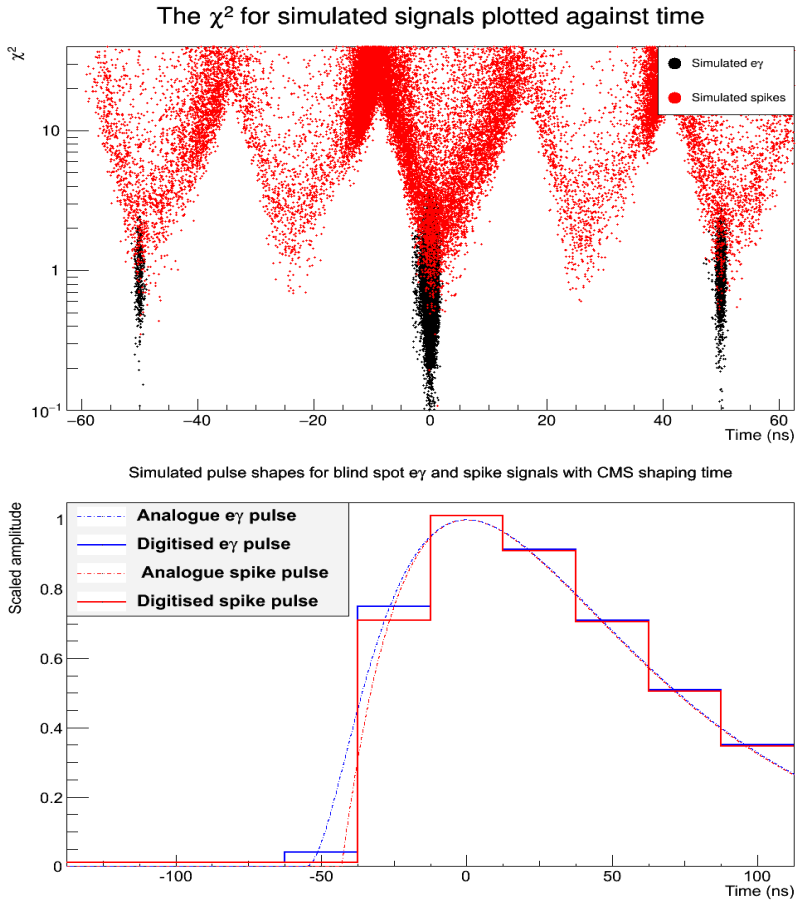

FIGURE 6.5: *Top:* The distributions of χ^2 for simulated $e\gamma$ and spike pulses are plotted against their reconstructed time. The periodic behaviour of the spike distribution is reproduced here. *Bottom:* simulated $e\gamma$ and spike pulses from the blind spot are compared. The analogue pulses for the spike and $e\gamma$ signals are included to demonstrate the situation more clearly.

this case (optimal cut efficiencies: Equations 6.10, 6.11) are all somewhat better than those presented for CMS data in Figure 5.3.

$$\text{Simulated spike rejection efficiency} = 0.9537 \pm 0.0004 \tag{6.11}$$

$$\text{Simulated e}\gamma\text{ acceptance efficiency} = 0.9703 \pm 0.0003 \tag{6.12}$$

This is not critical in the studies presented in the next Chapter, where *relative* differences between different pulse shaping algorithms are examined. However, it remains to be studied. It is likely that this is due to the variation between pulse shapes in CMS, which are not simulated here, together with the effects of pileup (also not simulated) which would distort the pulse shapes from the ideal case. However, one should note that the

simulation tool developed here is sufficiently flexible that such effects can be incorporated and studied in the future.

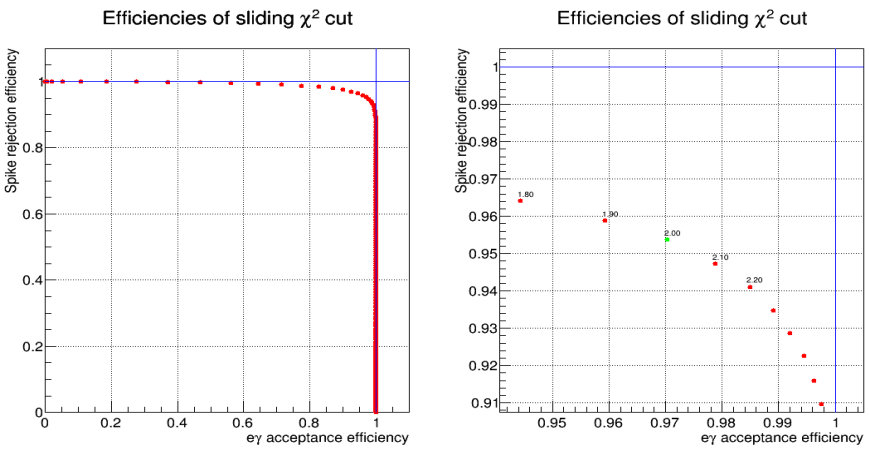

FIGURE 6.6: *Left:* Spike rejection efficiency of a sliding cut on the χ^2 distribution of simulated pulses is plotted against the $e\gamma$ acceptance efficiency. *Right:* Zoom on the top left corner of the plot on the left, the point closest to 100% efficiency is highlighted and the corresponding value of the χ^2 cut is displayed.

In summary, the pulse shape simulation has reproduced the general behaviour of CMS pulses and the periodic blind spot exhibited in the χ^2 distributions for CMS spikes. This tool can now be used to tune the conditions of the digitisation process to optimise the discriminating power of pulse shape based spike mitigation techniques.

The frustration level can get...quite high.

David Petyt, *Commenting on the CERN WiFi*

7

Optimisation of pulse shape discrimination using the Monte Carlo simulation

Following the development of the specialised pulse shape simulation tool, we are now in the position to investigate possible improvements to the pulse digitisation process to maximise spike rejection via pulse shape discrimination. These improvements include:

- New functionality that includes increasing the number of digitised samples and changing the electronic shaping time. These may be implemented when the ECAL front-end electronics are replaced in 2023 prior to HL-LHC running.
- Optimising existing settings by changing the digitisation phase. This can be implemented now without upgrading the electronics.

The current simulation tool allows all three of these parameters to be explored. Their effect on the spike rejection capabilities of ECAL will be investigated in this chapter.

7.1 Tuning the electronic shaping time

The electronics shaping function, shown in Equation 6.1, with characteristic shaping time τ_e, extends and shapes the analogue pulse from the APDs. The value of τ_e was

optimised to provide the best signal to noise ratio for the electronics noise currently present in CMS. There are several factors to consider when assessing whether to change the shaping time:

- A shorter shaping time accentuates the difference between spikes and $e\gamma$ pulses. This can be seen in Figure 7.1, which shows simulated spike and $e\gamma$ pulse shapes for three different values of $\tau_e = \{20 \text{ ns}, 43 \text{ ns}, 66 \text{ ns}\}$. This may improve the discriminating power of pulse shape variables in rejecting spikes.
- At the high pileup values expected at the HL-LHC[24], the probability of having overlapping pulses in the same channel will increase. This will distort the pulse shape and negatively affect pulse shape reconstruction and discrimination. This effect can be reduced by shortening the shaping time, effectively reducing the *spill over* between consecutive 25 ns time samples.
- Altering the shaping time changes the level of electronic noise in each digitised sample. The relationship between noise and shaping time is as follows:

$$\sigma_{\tau_e} = \sqrt{(0.025)\sigma_{43}^2 \left(\frac{43}{\tau_e}\right) + 0.47 \left(\frac{\tau_e}{43}\right) (I_d)} \tag{7.1}$$

Where $\sigma_{43} = 60$ MeV represents the current level of noise at CMS in MeV and τ_e is the electronic shaping time in ns. I_d represents what is referred to as *dark current* in the APDs in units of μA.

The two terms in this equation have different τ_e dependence. The first term, which is constant in time, is inversely proportional to τ_e. The second term, which increases with integrated luminosity is proportional to τ_e. The optimisation of τ_e therefore depends on the relative size of these two terms. Since it will not be possible to change the shaping time before 2023, one should consider the value of these two terms under HL-LHC conditions.

The dark current I_d results from radiation damage due to neutron irradiation of the APDs as they age and the LHC ramps up in luminosity. APDs, as well as all other diodes, suffer from dark current when the depletion region within their PN junction develops defects within the lattice. The consequence of this is the increased rate of the generation of random electron-hole pairs which act as charge carriers through the depletion region. Due to the existing reverse bias applied to the APDs, these charge carries form a constant current (I_d). This current increases as the lattice is damaged due

to neutron irradiation at the LHC in high radiation environments and so the value of I_d increases with total integrated luminosity[25].

Table 7.1 summarises the noise expected for three different values of τ_e and for two values of I_d: First the current (2012) conditions where $I_d \approx 0\ \mu A$, and second, the expected conditions during the running of HL-LHC where $I_d \approx 100\ \mu A$. It is clear that the optimal choice of τ_e for the best noise performance strongly depends on the value of I_d, with a shorter shaping time being beneficial for the large values expected in 2030[1].

	Digitisation noise (MeV)	
τ_e (ns)	$I_d \approx 0\ \mu A$ (2012)	$I_d \approx 100\ \mu A$ (2030)
66	48	340
43	60	280
20	88	200

TABLE 7.1: A summary of the effect of dark current (I_d) and electronic shaping time (τ_e) on the APD noise. The dark current values of 2012 and that predicted in 2030 during the High Luminosity phase of the LHC are listed for three different values of shaping time. The information for 2030, as well as for the 20 ns and 66 ns shaping times are extrapolated using Equation 7.1.

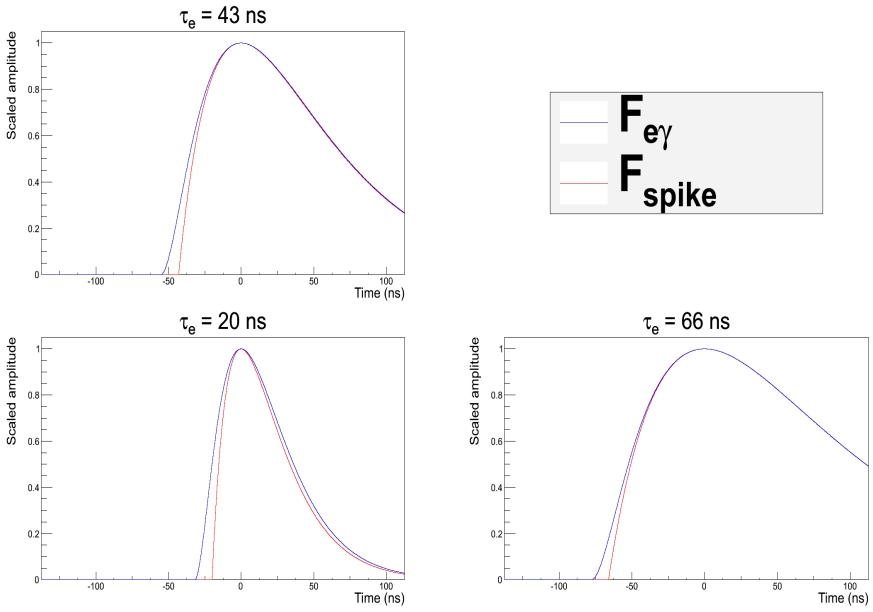

FIGURE 7.1: Simulated analogue pulses for 3 different shaping times are plotted. The larger the shaping time, the smaller the difference between $e\gamma$ and spike pulses.

The effectiveness of changing the shaping time on spike rejection can be seen in Figure 7.2. Here the spike rejection efficiency is plotted against transverse energy for three values of τ_e and for two values of I_d (top plot: 0 μA, bottom plot: 100 μA). The spike rejection efficiency at each point in the plot is computed at the value of χ^2 that yields 98% $e\gamma$ acceptance efficiency.

[1]The HL-LHC will begin running in 2025 after the end of the upgrade starting in 2023. The values used in this study are those expected after several years of HL-LHC running.

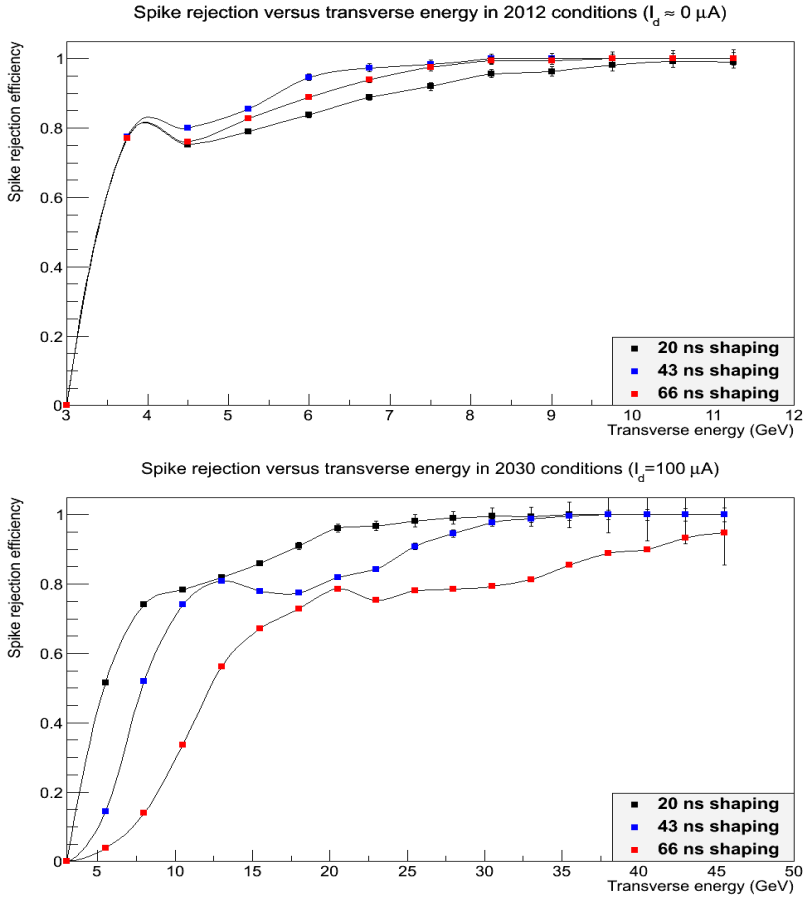

FIGURE 7.2: *Top:* The spike rejection efficiency of the χ^2 distribution for pulses produced by the APD with $I_d \approx 0\ \mu A$ (corresponding to CMS 2012 conditions) is plotted against transverse energy. The minimum $e\gamma$ acceptance efficiency is set to be at least 98%. *Bottom:* The same as the plot on top with $I_d = 100\ \mu A$ as predicted for the High Luminosity stage of the LHC in 2030[13].

The top plot of Figure 7.2, which is for the current I_d conditions, displays that there is no advantage in reducing the shaping time. Here, the larger difference in pulse shapes between spikes and $e\gamma$ signals is counteracted by the increased noise. This is not a particular issue, since it is not possible to modify the shaping time until 2023, however it shows that the existing shaping time of 43 ns is about optimal for the current LHC conditions.

The bottom plot of Figure 7.2 shows that a shorter shaping time is indeed beneficial for the noise conditions expected during HL-LHC[13]. This is because of the lower digitisation noise reported in the right-hand column of Table 7.1. The figure shows that a shaping time of 20 ns performs considerably better than $\tau_e = 43$ or 66 ns in conditions where the dark current dominates the overall electronic noise.

Finally, an interesting side effect of changing the shaping time is shown in Figure 7.3. This figure displays the efficiency curves for $\tau_e = 43$ and 20 ns, within the collision time

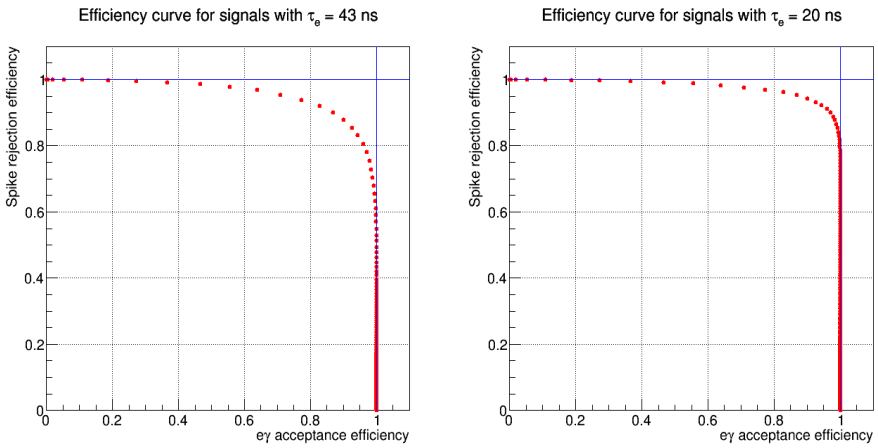

FIGURE 7.3: *Left:* Spike rejection efficiency of a sliding χ^2 cut is plotted against $e\gamma$ acceptance efficiency for signals within the collision time windows for $\tau_e = 43$ ns as was the case in 2012. *Right:* The same as the plot on the left with a shaping time of $\tau_e = 20$ ns.

windows ($|t_{rec} - t_{col}| < 3$ ns). Here a shorter shaping time produces better spike rejection and $e\gamma$ acceptance probabilities. This means that in this region of phase space, the larger shape difference with a smaller shaping time (Figure 7.1) provides a net benefit.

7.2 Optimising the digitisation phase

During the analysis of 2012 data (Chapter 5), altering the digitisation phase of the pulses was one of the solutions suggested to move the blind spot of the χ^2 away from $t = 0$ ns. The optimal phase is found by minimising the overlap between spikes and $e\gamma$ signals in the 2D plane of χ^2 versus reconstructed time. This is demonstrated in Figure 7.4 where the current phase is used in the top plot and the optimal phase is used in the bottom plot.

As expected, the optimal digitisation phase fully separates spikes from $e\gamma$ signals. This is achieved with a total phase shift of $\Delta t = -9$ ns compared to the current digitisation phase.

The spike rejection versus $e\gamma$ acceptance curves for the current and optimal digitisation phase for signals within the collision time windows are shown in Figure 7.5. The pulse shapes are digitised with the same shaping time and number of samples as in CMS data during 2012. Here once can see that for data within the collision time windows, the inefficiency due to the blind spot is completely eliminated when the optimal phase is applied.

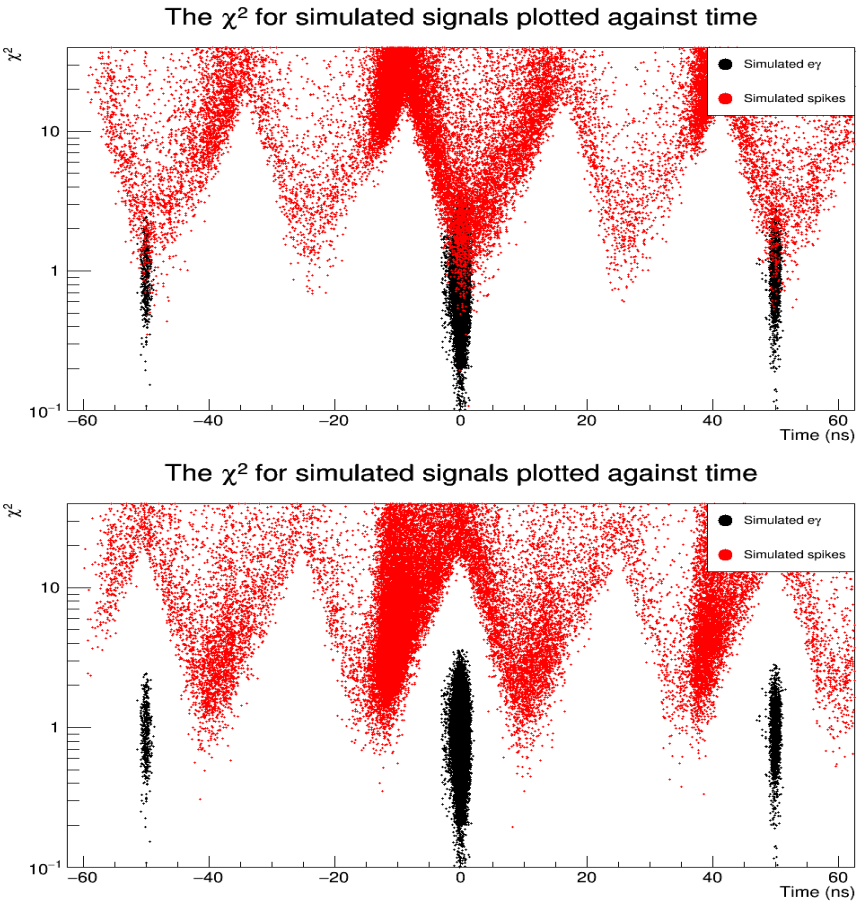

FIGURE 7.4: *Top:* The behaviour of the χ^2 distribution against time for simulated pulses with the nominal digitisation phase of $t_1 = 2$ ns. *Bottom:* The same as above with an optimised digitisation phase of $t_2 = -7$ ns resulting in a total $\Delta t = -9$ ns phase shift.

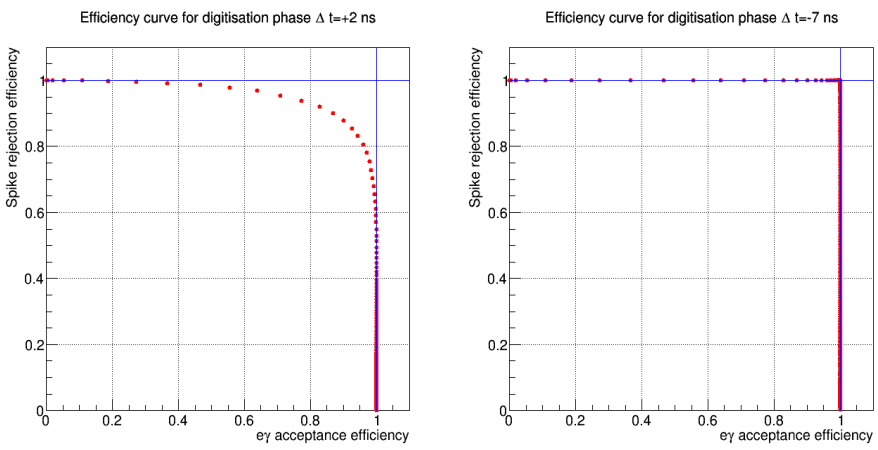

FIGURE 7.5: *Left:* Spike rejection efficiency of a sliding χ^2 cut is plotted against $e\gamma$ acceptance efficiency for signals within the collision time windows for pulses digitised with a phase of $t_1 = 2$ ns as was the case in CMS in 2012. *Right:* The same as on the left with the digitisation phase optimised with $t_2 = -7$ ns resulting in a total $\Delta t = -9$ ns phase shift.

The process of optimising the digitisation was repeated with a shorter shaping time of $\tau_e = 20$ ns. Here it was found that the blind spot could be eliminated with a smaller phase shift of $\Delta t = -7$ ns relative to the current phase. This is a relevant difference since there will be a trade-off between the optimum phase needed for spike rejection and that required for the optimal amplitude reconstruction of signals in the ECAL trigger (see discussion in Chapter 6).

7.3 Increasing the number of digitised samples

As Figure 6.5 demonstrated, the blind spot is a consequence of the scarcity of the number of digitised samples since the pulse shapes prior to digitisation are clearly different (Figure 6.2). By increasing the number of samples from 10 to 20, the distribution of χ^2 for simulated spikes pulses is moved further from that of $e\gamma$ pulses. This is clearly demonstrated in the top plot of Figure 7.6, which shows almost complete separation between the spike and $e\gamma$ χ^2 distributions. Furthermore, in the bottom plot which shows the dependence of χ^2 on reconstructed time, the blind spot is completely removed. Note that since there are now 2 measurements in each 25 ns period when 20 samples are used, the periodicity of the χ^2 distribution is halved.

The improvement in spike rejection from doubling the number of samples is shown in Figure 7.7, which plots the spike rejection efficiency versus $e\gamma$ acceptance for pulses with 10 digitised samples (left) and 20 digitised samples (right). All other variables (digitisation phase and shaping time) are fixed to their default values. One can clearly see that it is possible to achieve 100% spike rejection with 100% $e\gamma$ acceptance for all signals if 20 samples are used.

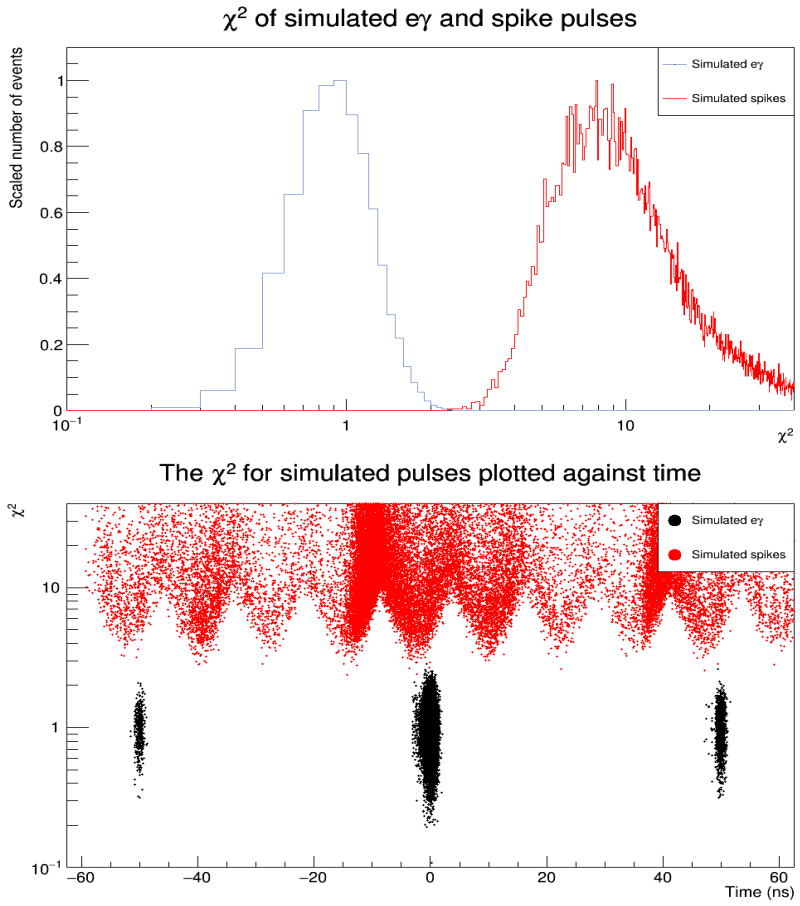

FIGURE 7.6: *Top:* The χ^2 distributions of simulated spikes and $e\gamma$ signals are plotted for signals with 20 digitised samples. The χ^2 distribution for simulated $e\gamma$ pulses are almost completely separated from that of the simulated spikes when the number of samples is increased from 10 to 20. *Bottom:* The χ^2 distributions for spikes and $e\gamma$ signals are plotted against time for signals with 20 digitised samples. The spike χ^2 drop period is half that of CMS in this case and the blind spots no longer exist.

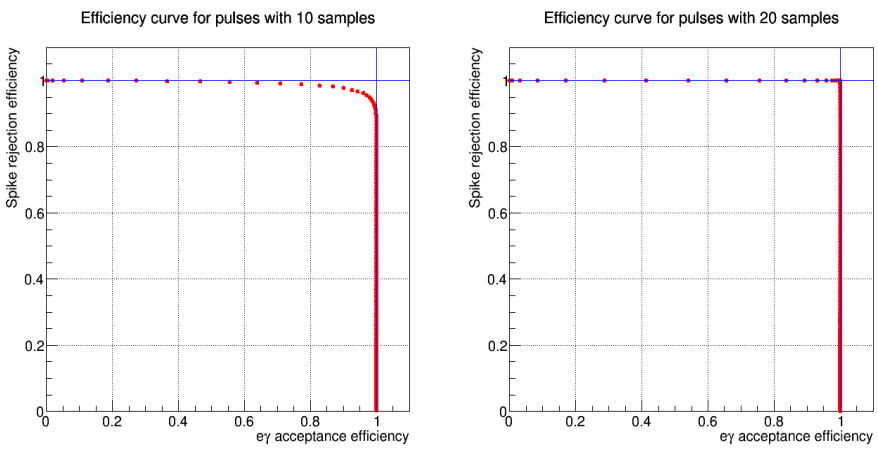

FIGURE 7.7: The effect of changing the number of samples on the efficiency curves of the χ^2 variable are plotted. *Left:* Efficiency of χ^2 of simulated pulses with 10 samples per digitised pulse. *Right:* Same as the left with 20 samples per digitised pulse.

I done wrestled with an alligator, I done tussled with a whale; handcuffed lightning, thrown thunder in jail; only last week, I murdered a rock, injured a stone, hospitalised a brick; I'm so mean I make medicine sick.

Mo Farzanehfar, *Quoting Mohammed-Ali Clay*

8

Analysis of results and conclusion

In this chapter a summary of the work will be presented and the proposed pulse shape dependant spike mitigation solutions will be analysed on a cost/benefit basis. These will be evaluated based on the effect they have on the spike triggering rates of L1 (Table 2.1) as was done for existing mitigation methods in Chapter 4. This analysis will be followed by concluding remarks on the current work, as well as a proposal for the future study of spike mitigation in the CMS barrel ECAL.

8.1 Summary

The occurrence of spikes in the CMS barrel ECAL reduces the available bandwidth of the Level-1 and HLT triggers for good events (Table 2.1). This rate reduction, if ignored, would dramatically affect the performance of CMS event reconstruction and energy resolution for any and all interactions involving electrons or photons in the final state (Chapter 2). It was discovered that the anomalous signals result from direct ionisation of the APDs by charged hadrons resulting from interactions in LHC collisions. Many of these hadrons are end products of processes occurring within the protective epoxy coating that exists between the APDs and the $PbWO_4$ crystals (Figure 3.1).

Two of the three properties of spikes, namely their energy topology and reconstructed time (Chapter 3) have been previously used to mitigate the rates of spike triggering at L1 and HLT[6, 15]. However, it was found that the combination of these two techniques does not cover the full range of phase space. There exists a region when the signal pulses have a reconstructed time coincident with LHC collisions, where the existing methods are less efficient (Figure 4.4).

This report has presented the potential of using a third property of spikes, their pulse shape, in developing new and improved techniques for spike mitigation.

Using the χ^2 statistic to differentiate between $e\gamma$ and spike pulses in CMS data, it was found that in certain cases, there are not enough samples in the digitised pulse to separate the two. This combined with the relative phase at which CMS decides to digitise pulses (Figure 6.1), causes the χ^2 statistic to develop a periodic blind spot where $e\gamma$ pulses and spike pulses are identical to within errors (Figures 5.4, 5.5).

Since the location of these blind spots depends on several parameters of the digitisation process (Figure 6.1), a special pulse shape Monte Carlo simulation was developed to study the effect of altering each parameter, either individually or in combination (Chapter 6). This specialised tool was first benchmarked by replicating the features observed in CMS data. It was then used to optimise the digitisation parameters to maximise spike/$e\gamma$ separation in χ^2 space. The Monte Carlo was used to study the effect of altering the electronic shaping time, the digitisation phase of the analogue pulses, and the number of samples per digitised pulse.

The results from these studies were presented and analysed briefly in the context of spike rejection and $e\gamma$ acceptance efficiencies for each of the three parameters listed above. A summary of these results and an assessment of their potential implementation in CMS will be presented in the next section.

8.2 Analysis of proposed solutions

8.2.1 The electronic shaping time

Reducing the electronic shaping time has two effects:

- It increases the shape difference between spike and $e\gamma$ pulses (Figure 7.1)
- It changes the level of electronic noise per digitised sample (Equation 7.1)

It was found that the critical variable determining the optimal value of the shaping time is the APD dark current (I_d in Equation 7.1). For large values of this parameter, expected during HL-LHC running, it is seen that the second term in Equation 7.1 dominates and that a shorter shaping time is preferred. This is demonstrated clearly in Figure 7.2, which shows that a 20 ns shaping time is better than the existing 43 ns shaping time for spike rejection under HL-LHC running conditions.

For existing conditions (small I_d) the improved shape difference for a shorter shaping time is cancelled out by the increased noise predicted by Equation 7.1. However, since changing the shaping time requires the full dismount of the ECAL supermodules and refurbishment of the on-detector electronics, such an operation is not possible until 2023, at the start of HL-LHC upgrade period.

Given these findings, reducing the electronics shaping time is preferable for the optimal operation of ECAL in the context of spike mitigation at HL-LHC.

8.2.2 The digitisation phase

The location of the periodic blind spot of the χ^2 statistic is due to the relative phase between the time of digitisation and the reconstructed time of incoming pulses. By appropriately altering the digitisation phase, it was demonstrated that the χ^2 mixing of simulated spikes and $e\gamma$ signals within the collision time windows is entirely circumvented (Figure 7.4).

For the existing CMS conditions where a +2 ns phase shift is already present, it was found that a total net phase shift of $\Delta t = -9$ ns is necessary to achieve optimal separation between $e\gamma$ and spike χ^2 distributions (Figure 7.5), thus allowing near 100% efficiency for both spike rejection and $e\gamma$ acceptance within the collision time windows. When a reduced shaping time of $\tau_e = 20$ ns is used, the net phase shift for full separation is reduced to $\Delta t = -7$ ns.

Studies of the digitisation phase suggest that for any shaping time an appropriate digitisation phase will eliminate all mixing between the χ^2 distributions of spikes and $e\gamma$ signals within the time windows of collision. This is only effective if timing information is also used in spike rejection, meaning that it is not effective at L1 (where no timing information can currently be used) and at the HLT (where no timing information is currently used). However, it can provide a benefit to offline reconstruction, where both timing, Swiss-Cross and χ^2 variables could be combined to reject spikes.

It is therefore useful to consider changing the digitisation phase for future LHC running, especially as it requires no hardware upgrade. For this, one must take care to ensure

that any change in phase does not significantly impact the amplitude reconstruction in the trigger. This means that a phase scan must be performed to determine an acceptable *compromise* working point that improves spike rejection without impacting trigger performance.

8.2.3 The number of digitised samples

The root cause of the blind spot phenomena in the χ^2 distribution of spike signals is the lack of enough digitised samples per pulse to distinguish between $e\gamma$ and spike pulses (Figure 6.5). The most straightforward solution is therefore to increase the number of samples.

It was found that doubling the number of samples from 10 to 20 results in $e\gamma$ and spike χ^2 distributions that are completely separated (see Figure 7.6). This showed that increasing the number of samples is a very powerful way of increasing the resolving power of ECAL to reject spikes.

However, increasing the number of samples (which is only possible when the ECAL electronics are refurbished in 2023 prior to HL-LHC) has other implications. Doubling the number of samples doubles the data volume. It has increased costs due to the larger number of readout fibres required and the additional computing resources to manage this bigger data size.

One logical extension of this result is to perform a shape test on the analogue pulse shape, *i.e.* within the front-end electronics before pulse digitisation has taken place. This is equivalent to having a very large number of digitised samples and can completely remove the blind spot problem discussed earlier. This could manifest itself as a pulse shape based discriminating *bit* which would use properties such as the energy and width at half maximum of the incoming analogue pulses to produce a spike flag. This spike-bit could take the following form:

$$\lambda = \frac{1}{2}\left(\left(\frac{\left|\frac{W_i}{E_i} - w_{ref}\right|}{\frac{W_i}{E_i} - w_{ref}}\right) + 1\right) \quad , \quad \frac{W_i}{E_i} \neq w_{ref} \tag{8.1}$$

Where λ is the spike checking bit. W_i and E_i represent the width at half maximum and the maximum energy of the incoming pulse respectively. w_{ref} represents the width at half maximum per energy of a reference intermediate pulse shape between typical $e\gamma$ and spike signals. This has to be optimised empirically. According to Equation 8.1, every time a pulse is narrower than the cut off pulse related to w_{ref}, the bit returns $\lambda = 0$ and

if it is larger the bit returns $\lambda = 1$ thus allowing L1 to reject all events with $\lambda = 0$ as spikes.

Such a bit which utilises pulse shape based discrimination methods would heavily benefit from the analogue pulses that exist prior to digitisation and so could solve the spike problem at the Level-1 trigger, or at the very least, heavily reduce the current spike rate that flows through to the HLT.

8.3 Conclusion

The cause of spikes in the CMS barrel ECAL and the current mitigation methods have been explored and summarised. It was found that of the three main properties of spikes, the pulse shape had not yet been directly exploited leaving the most interesting part of the phase space, namely, the collision time windows (Figure 4.4) with unmitigated spikes. Exploring the χ^2_{CMS} of pulses revealed a inherent periodic blind spot which affected pulses occurring within the collision time windows (Figures 5.4, 5.5).

During this research it was discovered, via the development of a detailed Monte Carlo simulation, that optimising the digitisation process results in significant improvement of spike mitigation within the collision time windows.

It was found that shortening the shaping time, together with an appropriate shift in the digitisation phase can completely solve this problem for the offline reconstruction of data (Figure 7.5) and potentially at the HLT as well. However, it does not affect the spike rates at the Level-1 trigger.

The most powerful effect was found by increasing the number of samples from 10 to 20. This allowed full discrimination between spike and $e\gamma$ pulses (Figures 7.4, 7.5). Implementing this in CMS directly would require doubling the current data bandwidth which which would have non-negligible implications on the design of the off-detector readout and data acquisition systems of CMS.

An alternative would be to develop a single discriminating bit (such as Equation 8.1) which would use the well-defined shape of analogue signals prior to digitisation to prevent triggering on spikes.

In conclusion, to maintain the excellent performance of the CMS barrel ECAL and allow it to continue to provide crucial physics data in a reliable manner, it is suggested that the electronic shaping time in the replacement ECAL electronics be reduced to $\tau_e \approx 20$ ns and the digitisation phase be altered by $\Delta t = -7$ ns from its current setting. This, in conjunction with a cut on reconstructed time and the Swiss-Cross variable, would

eliminate almost all of the current spike rate within the collision time windows depicted in Figure 4.4.

For the future, effort should be devoted to the development of a *spike-bit* that can be implemented in the replacement front-end electronics. This bit would exploit the difference in the analogue shapes of spike and $e\gamma$ pulses ($i.e$ before digitisation). From the existing studies, this should be a very powerful method in rejecting spikes. A proposed variable for such a bit is presented in Equation 8.1 to serve as a starting point for future work and the Monte Carlo framework developed in this study can be adapted to study its performance.

References

[1] D. Costanzo (2001), 0105033, URL http://arxiv.org/abs/hep-ex/0105033.

[2] L. Evans and P. Bryant, Journal of Instrumentation **3**, S08001 (2008), ISSN 1748-0221, URL http://stacks.iop.org/1748-0221/3/i=08/a=S08001.

[3] The ATLAS Collaboration, Physics Letters B **716**, 1 (2012), ISSN 03702693, URL http://www.sciencedirect.com/science/article/pii/S037026931200857X.

[4] The CMS Collaboration, Physics Letters B **716**, 30 (2012), ISSN 03702693, URL http://www.sciencedirect.com/science/article/pii/S0370269312008581.

[5] A. Benaglia, Journal of Instrumentation **9**, C02008 (2014), ISSN 17480221, URL http://stacks.iop.org/1748-0221/9/i=02/a=C02008.

[6] D. A. Petyt, Nuclear Instruments and Methods in Physics Research Section A: Accelerators, Spectrometers, Detectors and Associated Equipment **695**, 293 (2012), ISSN 01689002, URL http://www.sciencedirect.com/science/article/pii/S0168900211019553.

[7] The CMS Collaboration, Journal of Instrumentation **3**, S08004 (2008), ISSN 1748-0221, URL http://stacks.iop.org/1748-0221/3/i=08/a=S08004.

[8] *CMS online database*, https://cms-docdb.cern.ch (2013), accessed: 2015-05-10.

[9] A. Bartoloni, S. Baccaro, L. M. Barone, F. Cavallari, I. Dafinei, D. D. Re, M. Diemoz, E. D. Marco, M. Grassi, E. Longo, et al., Journal of Instrumentation **8**, C02039 (2013), ISSN 1748-0221, URL http://stacks.iop.org/1748-0221/8/i=02/a=C02039.

[10] A. Zabi, EPJ Web of Conferences **28**, 12036 (2012), ISSN 21016275, arXiv:1202.0594v1.

[11] P. Paganini, Journal of Physics: Conference Series **160**, 012062 (2009), ISSN 17426588.

[12] T. F. of Anomalous Signals in Calorimeters (Presented at a CMS Wednesday General Meeting on May 26, 2010), URL https://indico.cern.ch/event/81386/contribution/1/material/slides/1.pdf.

[13] P. Gras, Journal of Physics: Conference Series **587**, 012016 (2015), ISSN 1742-6588, URL http://stacks.iop.org/1742-6596/587/i=1/a=012016.

[14] K. Theofilatos, IEEE Nuclear Science Symposium Conference Record **03020**, 2065 (2012), ISSN 10957863.

[15] K. Theofilatos, in *2012 IEEE Nuclear Science Symposium and Medical Imaging Conference Record (NSS/MIC)* (IEEE, 2012), pp. 2065–2067, ISBN 978-1-4673-2030-6, ISSN 1082-3654, URL http://ieeexplore.ieee.org/lpdocs/epic03/wrapper.htm?arnumber=6551476.

[16] K. Deiters, Q. Ingram, and D. Renker (CMS Collaboration), Tech. Rep. CMS-NOTE-2010-016, CERN, Geneva (2010), URL http://cds.cern.ch/record/1316926.

[17] C. Jessop, D. Barney, F. Cavallari, W. Funk, M. Hansen, and D. Petyt (Presented during Upgrade Week on February 11 at CERN, 2015), URL https://indico.cern.ch/event/371315/contribution/2/material/slides/1.pdf.

[18] The CMS Collaboration, Journal of Instrumentation **5**, T03011 (2010), ISSN 1748-0221, URL http://cds.cern.ch/record/1223866/usage.

[19] D. Contardo and J. Spalding, Tech. Rep. CERN-RRB-2013-124, CERN, Geneva (2013), URL https://cds.cern.ch/record/1605208.

[20] K. Theofilatos and the CMS ECAL collaboration, Journal of Physics: Conference Series **293**, 012042 (2011), URL http://stacks.iop.org/1742-6596/293/i=1/a=012042.

[21] W. Press, S. Teukolsky, W. Vetterling, and B. Flannery, *Numerical Recipes: The Art of Scientific Computing* (Taylor and Francis, ltd., 1987), ISBN 0521431085, URL http://www.jstor.org/stable/1269484?origin=crossref.

[22] W. R. Leo, *Techniques for nuclear and particle physics experiments: a how-to approach* (Springer-Verlag Berlin Heidelberg, 1987), ISBN 3540173862.

[23] Tech. Rep. CMS-NOTE-2010-012, CERN, Geneva (2010), URL https://cds.cern.ch/record/1278160.

[24] A. Apollonio, M. Jonker, R. Schmidt, B. Todd, S. Wagner, and Others, INSPIRE p. TUPFI012 (2013), URL http://inspirehep.net/record/1337079.

[25] S. Baccaro, J. E. Bateman, F. Cavallari, V. Da Ponte, K. Deiters, P. Denes, M. Diemoz, T. Kirn, A. L. Lintern, E. Longo, et al., Tech. Rep. CMS-CR-1998-010. 1, CERN, Geneva (1998), URL http://cds.cern.ch/record/395153.

9

Links to relevant computing code

Here the piece of software that was used to generate each figure is included. All figures were produced by Root 5.32 and so are best reproduced using this version of Root. All pieces of computer code can be found on my public dropbox folder.

Below the label of each figure is linked to the name of the file which was used to generate it:

- Figure 3.2 $\longrightarrow$ **dissertationeventdisplay.c**
- Figure 3.3 $\longrightarrow$ **rep11.c**
- Figure 4.2 $\longrightarrow$ **interim5.c**
- Figure 4.3 $\longrightarrow$ **interim8.c**
- Figure 4.4 $\longrightarrow$ **rep12.c**
- Figure 5.1 $\longrightarrow$ **rep2.c**
- Figure 5.2 $\longrightarrow$ **rep4.c**
- Figure 5.3 $\longrightarrow$ **rep15.c**
- Figure 5.4 top $\longrightarrow$ **rep5.c**

- Figure 5.4 bottom ⟶ **rep16.c**
- Figure 5.5 ⟶ **rep6.c**
- Figure 6.2 ⟶ **rep7.c**
- Figure 6.3 ⟶ **simulation_dist.c**
- Figure 6.4 ⟶ **rep25.c**
- Figure 6.5 top ⟶ **rep20.c**
- Figure 6.5 bottom ⟶ **rep8.c**
- Figure 6.6 ⟶ **rep26.c**
- Figure 7.1 ⟶ **rep10.c**
- Figure 7.2 ⟶ **David_Plot2.c**
- Figure 7.3 left ⟶ **rep18.c**
- Figure 7.3 right ⟶ **rep17.c**
- Figure 7.4 top ⟶ **rep20.c**
- Figure 7.4 bottom ⟶ **rep19.c**
- Figure 7.5 left ⟶ **rep18_1.c**
- Figure 7.5 right ⟶ **rep21.c**
- Figure 7.6 top ⟶ **rep22.c**
- Figure 7.6 bottom ⟶ **rep23.c**
- Figure 7.7 left ⟶ **rep27.c**
- Figure 7.7 right ⟶ **rep24.c**

If there are any questions regarding this code I can be reached at:

- af1g11@soton.ac.uk
- ali.farzaneh.far@cern.ch
- ali.piadista@gmail.com